PFC/RR-82-21

DOE/ET-51013-51
UC-20

HIGH ENERGY ION DEPLETION IN THE CHARGE EXCHANGE SPECTRUM OF ALCATOR C

David Paul Schissel

Plasma Fusion Center
Massachusetts Institute of Technology
Cambridge, MA 02139

August 1982

This work was supported by the U.S. Department of Energy Contract No. DE-AC02-78ET51013. Reproduction, translation, publication, use and disposal, in whole or in part by or for the United States government is permitted.

HIGH ENERGY ION DEPLETION IN THE CHARGE EXCHANGE SPECTRUM OF ALCATOR C

by

DAVID PAUL SCHISSEL

B.S., UNIVERSITY OF WISCONSIN
(1979)

SUBMITTED TO THE DEPARTMENT OF
NUCLEAR ENGINEERING IN PARTIAL
FULFILLMENT OF THE
REQUIREMENTS FOR THE
DEGREE OF

MASTER OF SCIENCE

at the

MASSACHUSETTS INSTITUTE OF TECHNOLOGY

AUGUST 1982

Signature of Author David Paul Schissel
Department of Nuclear Engineering
August 6, 1982

Certified by Martin Greenwald
Dr. Martin Greenwald
Thesis Co-Supervisor

Certified by Lawrence M Lidsky
Prof. Lawrence Lidsky
Thesis Co-Supervisor

Accepted by _____
Prof. A. Henry
Chairman, Graduate Committee

TABLE OF CONTENTS

HIGH ENERGY ION DEPLETION IN THE CHARGE EXCHANGE SPECTRUM OF ALCATOR C

by

David Paul Schissel

Submitted to the Department of Nuclear Engineering
on August 6, 1982 in partial fulfillment of the
requirements for the Degree of Master of Science in
Nuclear Engineering

ABSTRACT

A three-dimensional, guiding center, Monte Carlo code is developed to study ion orbits in Alcator C. The highly peaked ripple of the magnetic field of Alcator is represented by an analytical expression for the vector potential. The analytic ripple field is compared to the resulting magnetic field generated by a current model of the toroidal plates; agreement is excellent. Ion-Ion scattering is simulated by a pitch angle and an energy scattering operator. The equations of motion are integrated with a variable time step, extrapolating integrator.

The code produces collisionless banana and ripple trapped loss cones which agree well with present theory. Global energy distributions have been calculated and show a slight depletion above 8.5 keV. Particles which are ripple trapped and lost are at energies below where depletion is observed. It is found that ions pitch angle scatter less as energy is increased. The result is that, when viewed in velocity space, ions form "probability lobes" the shape of mouse ears which are fat near the thermal energy. Therefore, particles enter the loss cone at low energies near the bottom of the cone.

Recommendations for future work include improving the analytic model of the ripple field, testing the effect of $\nabla \cdot \boldsymbol{B} \neq 0$ on ion orbits, and improving the efficiency of the code by either using a spline fit for the magnetic fields or by creating a vectorized Monte Carlo code.

Thesis Co-Supervisor: Dr. Martin Greenwald

Title: Principal Investigator

Thesis Co-Supervisor: Prof. Lawrence Lidsky

Title: Professor of Nuclear Engineering

For my parents

I INTRODUCTION

This Master's thesis covers work done on the Alcator C tokamak at the MIT Plasma Fusion Center. In this paper, the main text is written as if the reader were familiar to tokamak physics, particle following, and specifically the Alcator design. For those who may require more information, the Appendices go into further detail.

Confinement time and plasma heating schemes are crucial issues confronting the fusion community. The effect of toroidal field ripple on ion orbits may play a fundamental role in the physics of τ_E and heating. This paper presents results of a three-dimensional, Monte Carlo, guiding center ion orbit code. Chapter II presents experimental data from both the Alcator A and C experiments. The diagnostic results discussed are from charge exchange and RF heating. This experimental data gives rise to the original motivation for this work. Chapter III gives an overview of the basic theory needed to write a computer code to follow ion orbits in high temperature plasmas. Such items as the guiding center equations of motion, neoclassical theory and ripple trapping theory are discussed in detail, while the physics of scattering and the charge exchange process are merely outlined. Chapter IV presents both the plasma modeling and computational methods and results. The plasma models include an analytical expression for the ripple magnetic field and an operator which scatters ions in both pitch angle and energy. The equations of motion are integrated with a variable time step, extrapolating integrator. The code produces collisionless banana and ripple trapped loss cones which are consistent with present theory. Global energy distributions have been calculated and show a a slight depletion at high energies. Those particles which are lost due to ripple trapping are observed to enter the loss cone at low energies. These low energy losses result from ions pitch angle scattering less as energy is increased. Chapter V presents recommendations for future work. Such recommendations include improving the analytic model of the ripple field, testing the effect of $\nabla \cdot \boldsymbol{B} \neq 0$ on particle orbits, and improving the efficiency of the code by either using a spline fit for the magnetic field or by creating a vectorized Monte Carlo code. Appendix A is a discussion of the Alcator tokamak. Appendix

B covers all mathematical derivations needed for this thesis, and Appendix C gives a detailed description of the Monte Carlo code used.

II MOTIVATION FOR WORK

II.1 Alcator A

In the later 1970's, depletion of high energy ions was observed by perpendicular charge exchange on Alcator A and reported by Greenwald[1]. The explanation for this depletion was that particles were being ripple trapped and ∇B drifting out of the machine. A critical energy for depletion was calculated for plasma conditions identical to those during lower hybrid heating. The energy was calculated to be 5 keV which agreed with experimental findings. Furthermore, experimental results showed a strong up down asymmetry in the ∇B direction. This depletion of particles creates a hole in velocity space which allow particles to pitch angle scatter into the loss cone and subsequently be lost. This effect could be very detrimental to RF heating.

At the same time that these measurements were being made, Gaudreau[2] was performing ICRF experiments, and Schuss[3,4] was performing lower hybrid heating experiments. In the first experiment, significant amounts of RF power were coupled to the plasma but no bulk heating was observed. A likely source of the problem was listed as ripple trapped particles. The lower hybrid experiment also had problems heating the bulk of the plasma. Both experiments created energetic tails, but no equilibration with the bulk was observed. Recent calculations by Schuss[5], using a one-dimensional Monte Carlo ion simulation technique, has shown that most of the RF power which was deposited into the plasma was lost due to ripple trapping.

Clearly, a more quantitative understanding of the ripple trapping and depletion in Alcator is extremely important. It was with this background that the idea of the present work was conceived. With the new RF experiment being placed onto Alcator C, it was decided to attempt to create a three-dimensional Monte Carlo code which would accurately simulate ion orbits in the tokamak.

II.2 Alcator C

In the fall of 1981, a ten channel neutral particle analyzer was placed on Alcator C. It immediately showed depleted spectra like that observed on Alcator A. In "low density" discharges ($\bar{n}_e < 2 \times 10^{14}\, cm^{-3}$), Fiore[6] has reported a depletion above 5 keV. Figure (1) shows a typical depleted spectrum. A vertical scan like that performed on Alcator A resulted in similar findings. Bromberg[7]has speculated that the ripple might be greater at the beginning of the toroidal discharge and then relax to a steady value after several seconds. This hypothesis was tested[6] by firing plasma discharges at different times with respect to the toroidal field flat top. Results showed a decrease in depletion as the plasma discharge was delayed. These results all tend to support the theory of ripple trapping in Alcator.

Rf heating experiments are being carried out on Alcator C but as of yet no definitive results have been attained.

Even though the original motivation for this work arose from the desire to explain the observed depletion of the charge exchange spectra on both tokamaks, it can be applied to a more general issue, namely that of energy confinement time. Arising out of the experiments on Alcator A was the "Alcator Scaling Law"

$$\tau_E \sim n a^2, \tag{1}$$

where τ_E is the energy confinement time, n is the plasma density and a is the minor radius. Recent confinement experiments on Alcator C have shown a more pessimistic time than predicted by Equation (1). The exact cause of this is not known but it is possible that ripple depletion could be playing a significant role. Whatever the reason, it is believed that modeling the ions in Alcator can lead to a better understanding of energy confinement.

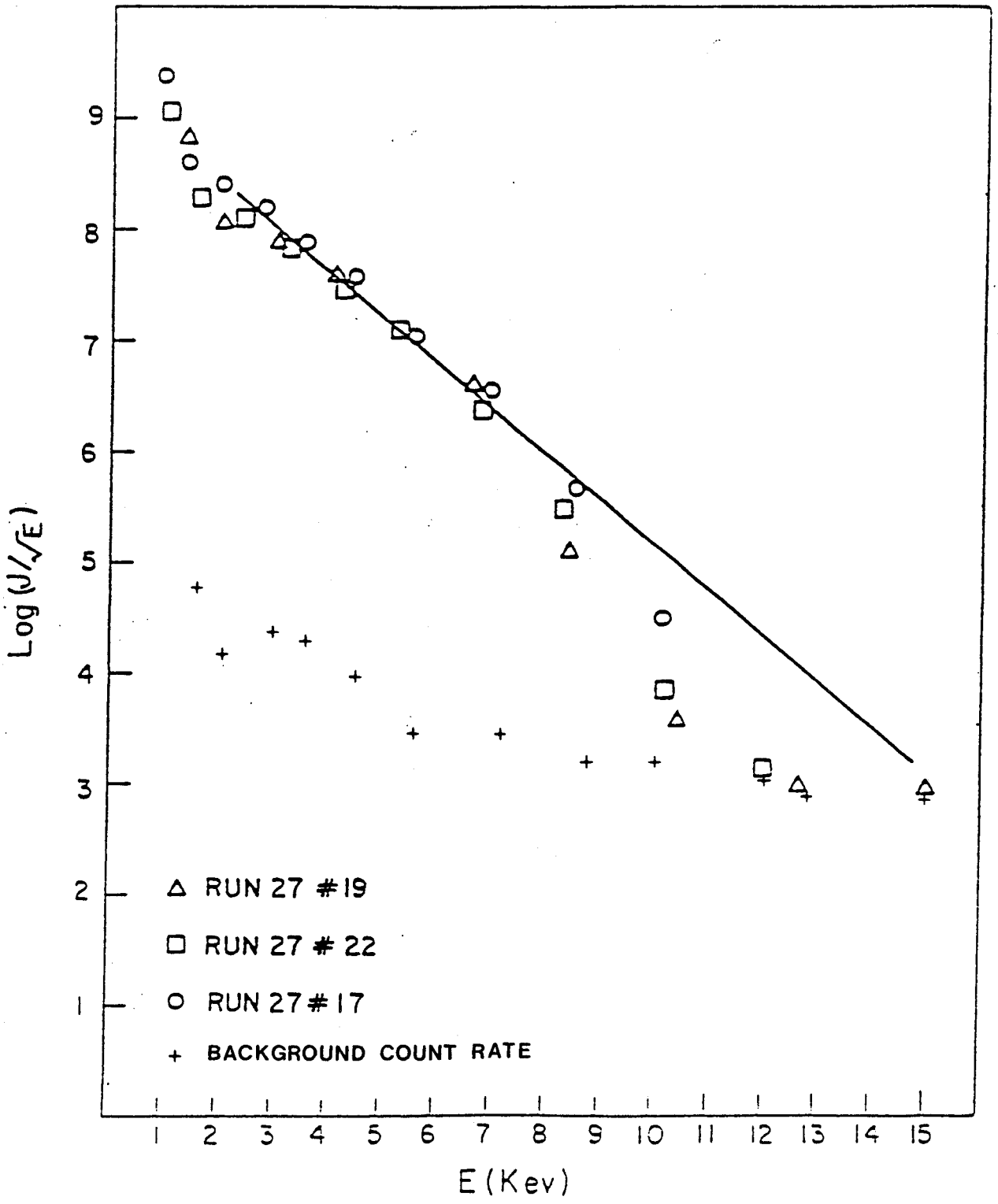

Fig. 1 — Shown is a typical depleted deuterium spectrum as seen by the perpendicular charge exchange analyzer on Alcator C. The straight line represents a Maxwellian temperature of 1.25 keV. $B_T = 8\,T$, $\bar{n}_e = 1.4 \times 10^{14}\,cm^{-3}$.

III BASIC THEORY

III.1 Guiding center equations of motion

When writing a computer code to track particle orbits, it is possible to follow the particle itself or its guiding center. Each method has its own particular advantages. In this work, I have decided to use the guiding center technique. There are two reasons for this choice. The first is that the phase information of the particle will not be needed. Implicit in this statement is the assumption that the effects of collisionless scattering in a ripple well are negligible when compared to the overall motion of an ion. The second reason is that since many computations will be required, and since the high frequency cyclotron motion of the particle is ignored, the guiding center method will allow larger time steps to be taken when compared to the particle following.

The coordinate systems used in this thesis are shown in Figure (2). The equations of motion and the ripple vector potential are transformed to the (R, ϕ, Z) system in order to ease the vector calculus calculations. The coordinate transformation is given by

$$(r, \theta, \phi) \Rightarrow \left(\left[Z^2 + (R - R_o)^2 \right]^{\frac{1}{2}}, \tan^{-1}\left(\frac{Z}{R - R_o} \right), \phi \right). \tag{2}$$

The guiding center equations are taken from Fowler[8]. Assuming that the fields are time independent, that the gravity force is small enough to be taken as zero, and that the electric field effects are small enough that they may be ignored, the guiding center equations in cgs units are

$$\frac{d\boldsymbol{R}}{dt} = \frac{c\boldsymbol{b}}{qB} \times \left(\frac{\mu \nabla \boldsymbol{B}}{c} + cmv_{\|}^2 \frac{\boldsymbol{b}}{B} \right) + v_{\|}\boldsymbol{b}, \tag{3}$$

and

$$\frac{dv_{\|}}{dt} = \frac{-\mu}{cm} \boldsymbol{b} \cdot \nabla B, \tag{4}$$

where

$$\boldsymbol{b} = \frac{\boldsymbol{B}}{B}, \tag{5}$$

$$\mu = \frac{1}{2}\frac{cmv_{\perp}^2}{B}, \tag{6}$$

$$v_{\parallel} = \frac{d\boldsymbol{R}}{dt} \cdot \boldsymbol{b}, \tag{7}$$

and

$$\frac{d\boldsymbol{R}}{dt} = \left(\frac{dr}{dt}, \frac{rd\theta}{dt}, \frac{-Rd\phi}{dt}\right). \tag{8}$$

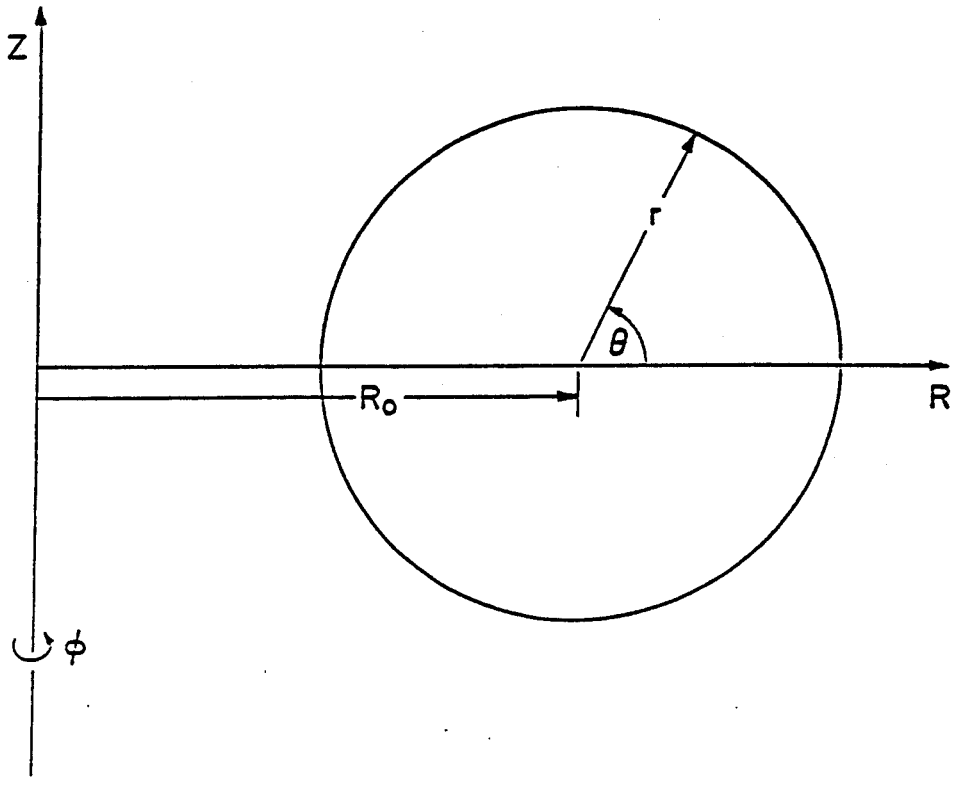

Fig. 2 — Axisymmetric toroidal geometry

III.2 Neoclassical theory

When a cylindrical magnetic field geometry is bent into a torus, "neoclassical" effects are observed. One of the effects is that a certain class of particles will become trapped, and their guiding centers will trace out orbits shaped like bananas when viewed in the poloidal plane. This trapping of particles occurs for the same reason as trapping occurs in a magnetic mirror. The trapped particles are small in number; approximately $(2r/R)^{1/2}$ is the fraction trapped at radius r. The time for a trapped particle to complete one orbit is called the bounce time and is given by $\tau_b \approx (R/r)^{1/2}(qR/v_\perp)$. The effective collision frequency for scattering out of the trapping region is $\nu_{eff} \approx (R/r)\nu$, where ν is the Braginskii 90° collision frequency:

$$\nu_i = \frac{4}{3}\pi^{1/2} n_i e^4 \ln\Lambda m_i^{-1/2}(kT_i)^{-3/2}, \tag{9}$$

$$\nu_e = \frac{4}{3}(2\pi)^{1/2} n_e e^4 \ln\Lambda m_e^{-1/2}(kT_e)^{-3/2}. \tag{10}$$

The concept of trapping becomes moot if the particle is scattered out of the trapping region before it has completed one orbit. If $\nu_{eff}\tau_b \gg 1$, trapping is irrelevant. The value $\nu_{eff}\tau_b$ is denoted $\nu^* = (R/r)^{3/2}\nu qR/v_{th}$ with $v_{th} = (kT/m)^{1/2}$.

The importance of trapped particle orbits arises when confinement is discussed. Classical collisions are binary coulomb collisions causing the particle to jump field lines by a step length of $\rho = (kT)^{1/2}m^{1/2}/eB$. The frequency at which these steps occur is just the Braginskii 90° collision time, so that the classical diffusion coefficient will be of order

$$D \approx \nu\rho^2. \tag{11}$$

When toroidal geometry is considered and trapped banana orbits occur, the step length increases to $\Delta r \approx \rho_p \epsilon^{1/2}$, which is the width of the banana. Here, ρ_p is the poloidal gyroradius and $\epsilon = r/R$. Thus transport is enhanced over the classical result. This type of cross field transport is called neoclassical transport.

To try to gain an understanding of this enhancement of diffusion, let us investigate the neoclassical diffusion coefficients. Historically neoclassical transport has been divided into three regimes. The first occurs when $\nu \ll \omega_b$ and thus particles will trace out several bananas before a scattering event occurs. Scattering out of the trapped region will occur in a time $\nu_{eff} \approx \nu/\epsilon$. The diffusion is dominated by the fraction $\epsilon^{1/2}$ which are trapped and occurs in time ν_{eff} over a step length equal to the banana width. Thus we have a diffusion coefficient of

$$D \approx \epsilon^{1/2} \nu \rho_p^2. \tag{12}$$

Comparing this with Equation (11), we see that when $\nu \ll \omega_b$, classical diffusion is enhanced by the factor $q^2\epsilon^{-3/2}$. Since banana orbits dominate this regime due to low collisionality it is called the "collisionless" or "banana" regime.

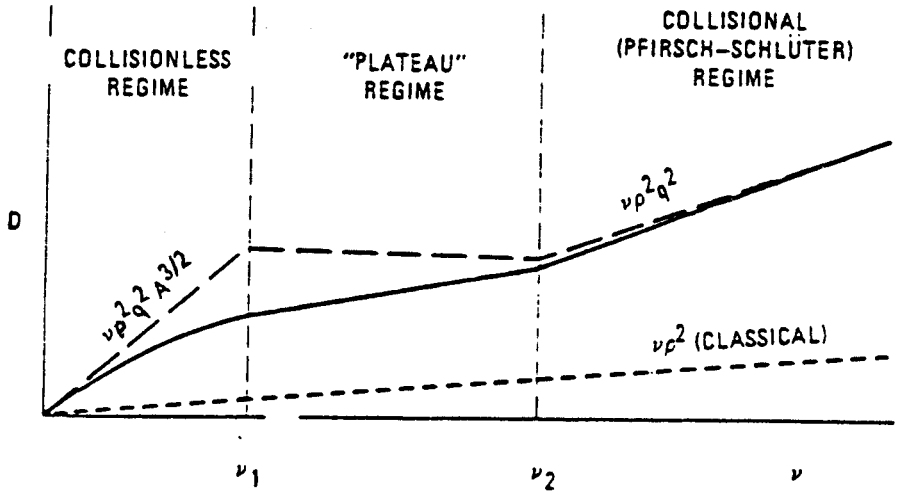

Fig. 3 — Schematic illustration of the dependence of the neoclassical diffusion coefficient on collision frequency.

The region of high collisionality is the "collisional" or "Pfirsch-Schluter" regime. Here $\nu \gg \omega_b$ and so collisions are too frequent to allow particles to complete one orbit. Due to the high collisionality, the time step is just the 90^o collision time, and thus

$$D \approx q^2 \nu \rho^2. \tag{13}$$

This coefficient is a factor q^2 larger than the classical answer.

The diffusion in the transition region is dominated by particles which are just barely trapped. Here $\nu_{eff} \approx \nu/\epsilon$ as in the banana regime, and the diffusion is that of the banana regime multiplied by the fraction of those particles slightly trapped. Thus

$$D \approx \rho^2 q v_{th}/R. \tag{14}$$

This regime is called the "Plateau" regime because the diffusion coefficient is independent of ν. The classic curve of D vs. ν is shown in Figure (3)[9].

III.3 Ripple trapping

Another way to lose ions is to have some of them become ripple trapped. Ripple of the magnetic field results because of the interruption of toroidal field coils at the diagnostic ports. Particles with small $v_\parallel$ can become trapped in the ripple well just as a certain class of particles can become banana trapped. Due to the drift velocity, v_D, these ripple trapped particles will drift upward until they are lost out of the machine or are scattered to higher $v_\parallel$ values. If the magnitude of the field ripple is $\Delta B/B \approx \delta \ll 1$, then the region of velocity space for trapping is given by $v_\parallel/v \approx \delta^{1/2}$. The diffusion coefficient can be calculated by noting that the fraction of ripple trapped particles is of order $\delta^{1/2}$; the diffusion coefficient will be of order $D \approx \delta^{3/2} v_D^2/\nu$ [9]. There does exist a regime where the collisionality is so low that the ripple trapped particles just drift straight out of the torus. In this regime the confinement time is just the time needed to collisionally scatter into the loss cone.

III.4 Physics of scattering

The scattering mechanism considered in this thesis is simple coulombic interactions. The Coulomb cross section for 90^o scattering due to many cumulative small-angle scattering events is

$$\sigma_{90^o} \approx \frac{2.6 \times 10^{-18}}{E^2}, \tag{15}$$

where E is the ion energy in keV and σ_{90^o} is in cm^2. The Coulomb cross section has a $1/v^4$ dependence so that more energetic particles will have a smaller collision frequency. The details of Rutherford scattering will not be presented here but they can be found in any elementary physics text.

III.5 Charge exchange process

The resonant charge exchange reaction is

$$\underline{H}^+ + H \Rightarrow \underline{H} + H^+, \tag{16}$$

where the underline refers to a high energy particle. A complete discussion of all of the relevant competing atomic processes is given by Cope[10]. Those readers who are interested in receiving a further understanding of how charge exchange is used to determine ion temperatures should refer to this work. The only item I wish to consider here is the relation between the calculation of a distribution function and the flux to the analyzer. In plasmas considered here, the charge exchange process is rare enough that it may be assumed not to bear any relevance to the evolution of distribution functions. Once the distribution function is obtained, the charge exchange process may be considered and the flux to the analyzer may be calculated. This flux I to the analyzer in units of $number/cm^3sec$ at $E \pm \Delta E/2$ is given by[11]

$$I = \frac{\sqrt{2}\Omega A}{\pi^{3/2}} \int_{-a}^{+a} \beta(x,E) n_o(x) n_i(x) \sigma_{cx}(E) v(E) m f_i \sqrt{E} \Delta E dx, \tag{17}$$

where β is the attenuation factor of neutrals through the plasma given by

$$\beta = e^{-\int_x^a n \sigma_T dx}, \tag{18}$$

dx indicates an integration along the line of sight,a is the plasma radius, σ_T is the cross section for any interaction to occur, Ω is the solid angle the detector sees, A is the beam area, n_o and n_i are the neutral and ion densities respectively, σ_{cx} is the charge exchange cross section, and f_i is the calculated ion distribution assumed constant over ΔE.

IV THEORETICAL COMPUTER STUDY

The first section of Chapter IV describes the model used to approximate the ripple of the magnetic field in Alcator. This ripple field is represented by an analytical expression for the vector potential. The next section presents the numerical integrator used to solve the equations of motion. This integrator is tested by plotting orbits for a magnetic field which is the sum of a pure toroidal and a poloidal field. Once the integrator is believed to be accurate, the ripple field is added on and the resulting ion orbits are studied. Section IV.3 presents the operators used to model ion-ion collisions. These collisions are simulated by scattering in energy and pitch angle. Section IV.4 takes the previous three sections and pulls them together to form one unified particle following code. In this section, the numerical methods needed to enable the code to run efficiently are discussed. Finally, the last section presents the results of the code. Energy and pitch angle distributions are presented as well as a study of loss cones in velocity space.

IV.1 Ripple model

There have been many papers published which use analytical expressions for the ripple of the magnetic field in tokamaks[12,13]. The most common expression used is of the form

$$B_\phi \approx \frac{B_o}{(1+\epsilon\cos\theta)}(1-\delta(r)\cos n\phi). \tag{19}$$

Here, $\epsilon = r/R$,n is the number of diagnostic ports, and $\delta(r)$ is a measure of the magnitude of the ripple. Unfortunately this expression and others like it are not divergence free and has a smooth sinusoidal variation of the ripple. The toroidal variation of the ripple in Alcator is highly peaked and a more complicated expression for the ripple must be used. Furthermore, it was felt that the divergence free nature of the analytical model might be important and thus a divergence free field was considered necessary. The author tried to adjust several of the numerous expressions that can be found in the literature but it is extremely difficult to create a ripple model that fits Alcator and, at the same time, is divergence free. If the

ripple could be generated from a vector potential, it would ensure that the resulting field would be divergence free. Once the vector potential A for the ripple is obtained, the total magnetic field may be written as

$$B = B_{pure} + B_{rip}, \tag{20}$$

with

$$B_{rip} = \nabla \times A. \tag{21}$$

B_{pure} is the sum of the $1/R$ toroidal field and of the poloidal field generated by the plasma current.

Using the vector potential of a mirror machine as a model, an initial guess was made at the desired vector potential. This expression was adjusted by varying some parameters and adding others until after many iterations the following vector potential was generated;

$$A = B_o\delta\left[r + \frac{r^t}{a^{t-1}}\right]\left(\cos\theta\hat{Z} - \sin\theta\hat{R}\right)\cos^m(n\phi). \tag{22}$$

In this expression, $\hat{Z}$ and $\hat{R}$ are unit vectors in the R and Z directions respectively, while the terms δ,t,m and n are parameters that may be varied in order to give the ripple field its desired shape and size. The $\cos^m(n\phi)$ term gives the ripple the necessary periodic feature and at the same time allows control of how peaked the ripple well will be. The $\left(\cos\theta\hat{Z} - \sin\theta\hat{R}\right)$ term gives the ripple a circular nature when viewed in the poloidal plane. The combination term of $\left[r + r^t/a^{t-1}\right]$ assumes that the ripple will be nonzero on axis.

Because they provide the best fit to the Alcator magnetic field, the values of $\delta = .005$,$t = 3$,$m = 10$, and $n = 3$ are used in the computer model. It should be noted that Alcator has six diagnostic ports but due to the fact that the cosine term is raised to a power, n is only half of 6. Figures (4- 6) are ripple contour plots of

$$\frac{B - \frac{B_oR_o}{R}}{\frac{B_oR_o}{R}}. \tag{23}$$

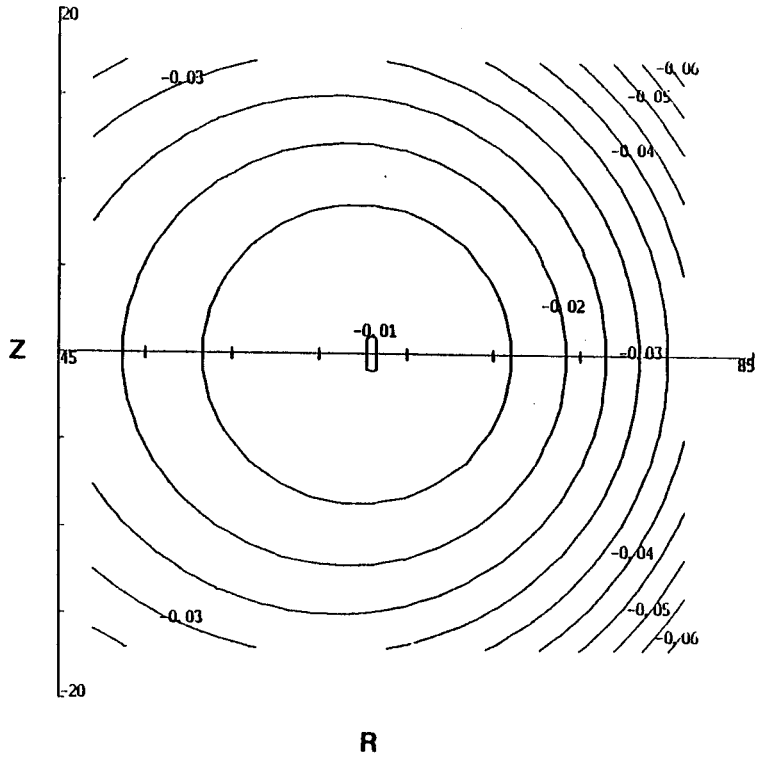

Fig. 4 — Poloidal view of ripple contour at $\phi = 0$.

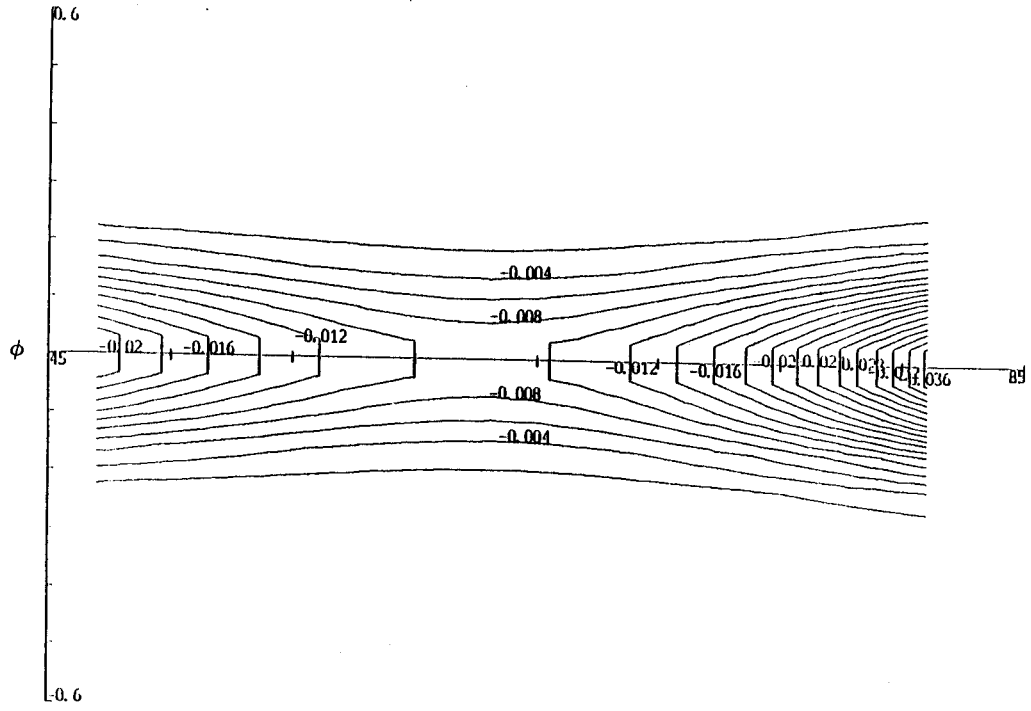

Fig. 5 — Ripple contour in the $R\phi$ plane at $Z = 0$.

Figure (4) is a ripple contour plot in the poloidal plane at $\phi = 0$. Figure (5) is a ripple contour plot in the $R\phi$ plane at $Z = 0$. Figure (6) is an enlargement of Figure (5).

Bromberg[7] has used a two-dimensional model to simulate the current distribution in the Bitter plates of Alcator. The resulting current distribution is used to generate the toroidal field ripple. The ripple from his model is shown in Figures (7) and (8). These figures should be compared to Figures (4) and (6). As can be seen, agreement is quite good. The most noticeable discrepancy is that Figure (7) has a ripple which is off center. This effect has not been produced in the present analytical model, as it is felt that the deviation from center has a small effect on particle orbits. Furthermore, Figure (8) shows points of positive ripple or overcompensation. Since the positive bumps are quite small compared to the negative ones, this effect is also believed to be insignificant.

The fact that the ripple component of the magnetic field was generated from a vector

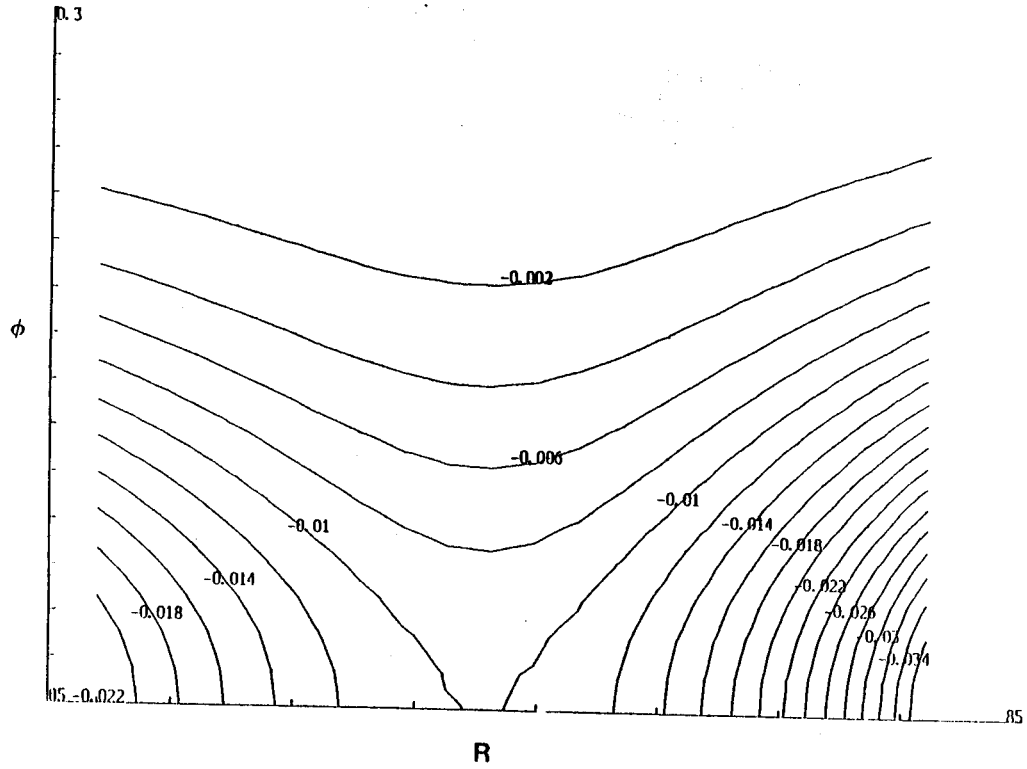

Fig. 6 — Enlarged view of the ripple contour as shown in Figure (5).

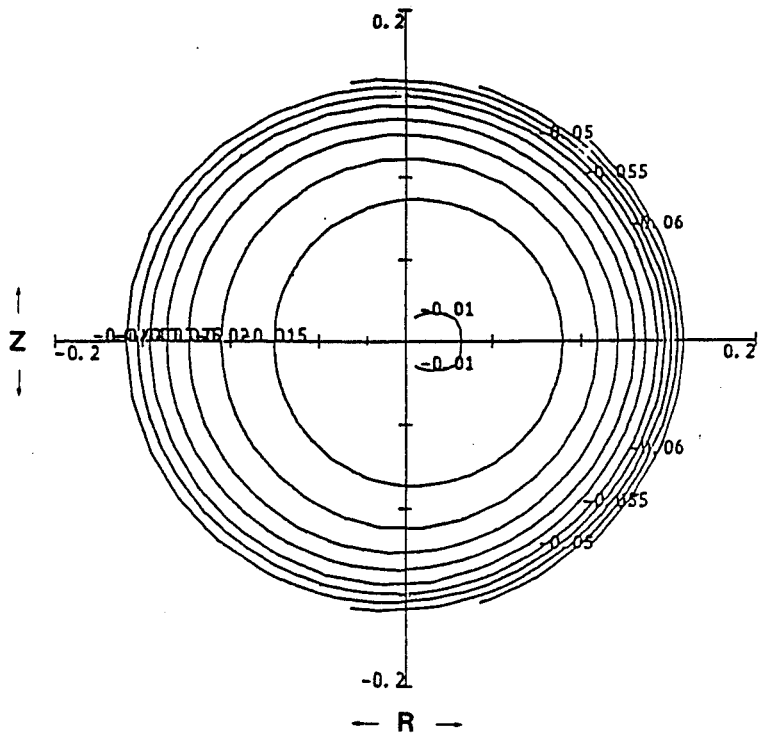

Fig. 7 — Poloidal view of Ripple contour at $\phi = 0$ generated from Bromberg's two-dimensional current distribution model.

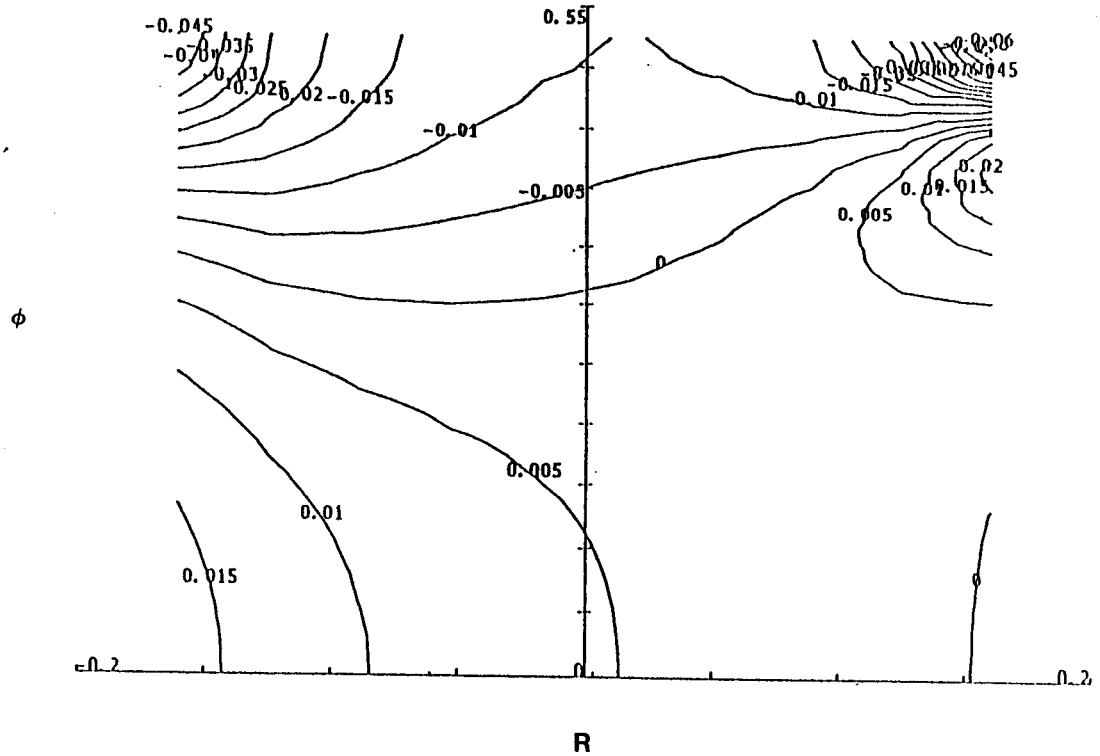

Fig. 8 — Ripple contour in the $R\phi$ plane at $Z = 0$ generated from Bromberg's two-dimensional current distribution model.

potential ensured that the field will be divergence free. Unfortunately the same can not be said about the curl of B_{rip}. If the curl of B_{rip} is not zero, it is important to know the direction and magnitude of these implied currents since they could perturb ion orbits and alter the numerical results. The implied current, $J_{implied}$, is generated from

$$J_{implied} = \frac{1}{\mu_o} \nabla \times B_{rip}, \tag{24}$$

and has a direction which is only in the poloidal plane. Figure (9) is a contour plot of $J_{implied}$ in the $R\phi$ plane at $Z = 0$. The maximum implied current is at the inner limiter edge and is approximately $20\, kA/m^2$. Figure (10) is a contour plot of $J_{implied}$ in the poloidal plane at $\phi = 0$. Here the largest current implied in the magnets is $2000\, kA/m^2$. The current density in the toroidal field coils is approximately $8 \times 10^5 kA/m^2$ yielding a ratio of implied to actual of $1/400$. Thus the implied current will only cause a small perturbation on the toroidal field. The maximum plasma current density is $10\, MA/m^2$ at the center. Assuming that the current falls by e^{-4} at the edge, the density becomes $180\, kA/m^2$. This yields a ratio of implied current to plasma current of 1/10. As we proceed from the edge inward, the ratio improves to approximately 1/10000 at the center. We conclude that the implied current is small enough so that the curl of B_{rip} may be assumed negligible.

To gain more insight into the effects of ripple and to further test the computer code, the ripple field was added to the existing code with the plotting routine and an analysis of individual particles was done. An example of a particular particle is shown in Figure (11). This "smoking banana" results from an ion which is trapped in a precessing banana orbit until its tip lands in a ripple well, is ripple trapped, and is subsequently lost. Note how the ripple has the effect of causing the banana orbit to wander. Comparison of Figure (11) to a case where the ripple has been nulled out, as in Figure (12), will convince the reader that the wandering of the banana orbit is definitely a ripple effect and not one of numerical error.

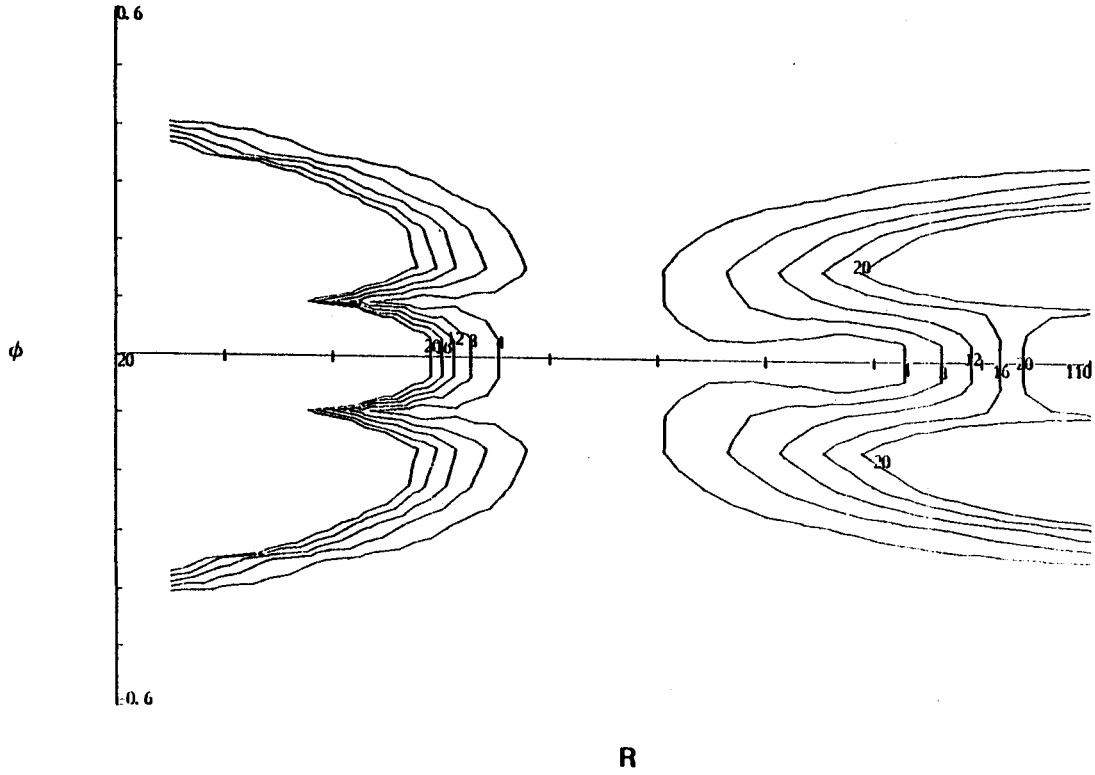

Fig. 9 — Contour plot of the implied current generated by the analytical ripple field as viewed in the $R\phi$ plane at $z = 0$.

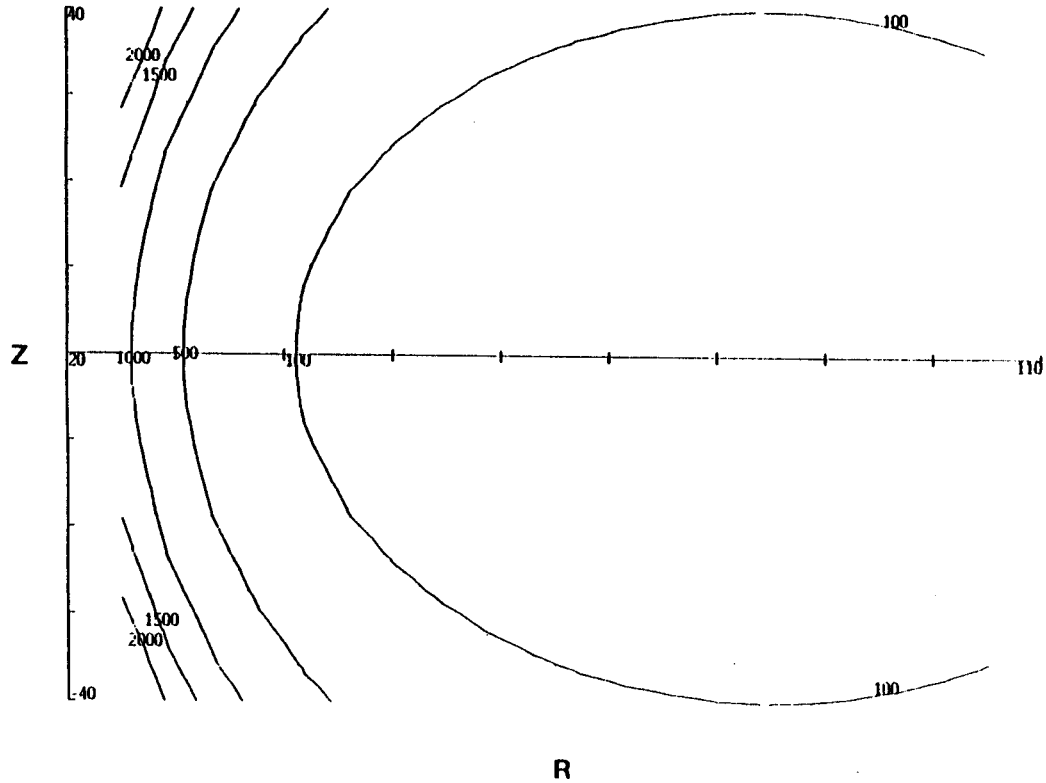

Fig. 10 — Contour plot of the implied current generated by the analytical ripple field as viewed in the poloidal plane at $\phi = 0$.

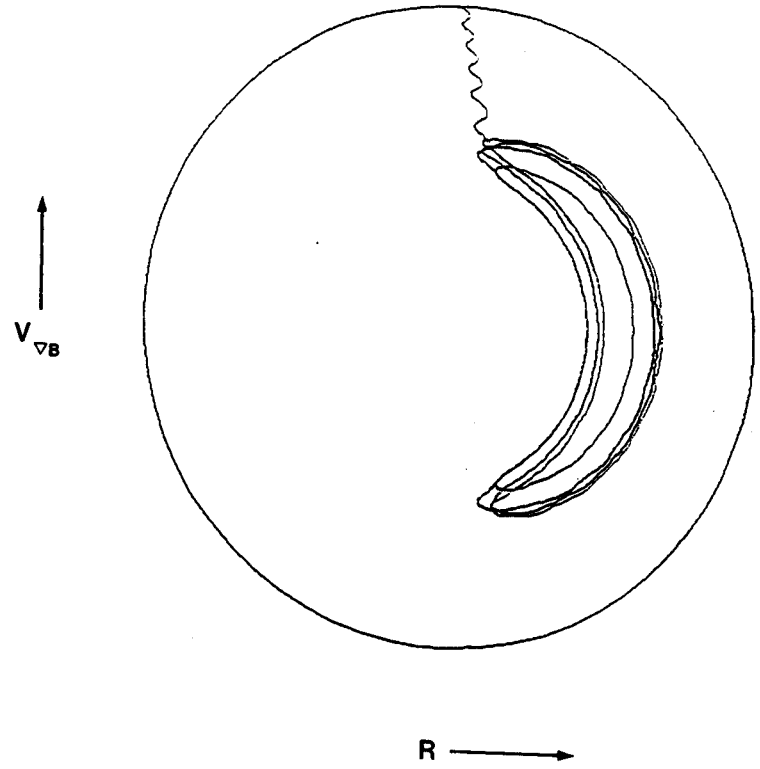

Fig. 11 — "Smoking Banana"-Banana orbit with standard Alcator ripple for a 52.2 keV hydrogen ion. $B_T = 8\ T, q_l = 4, q_o = .9,\ a = 17\ cm.$

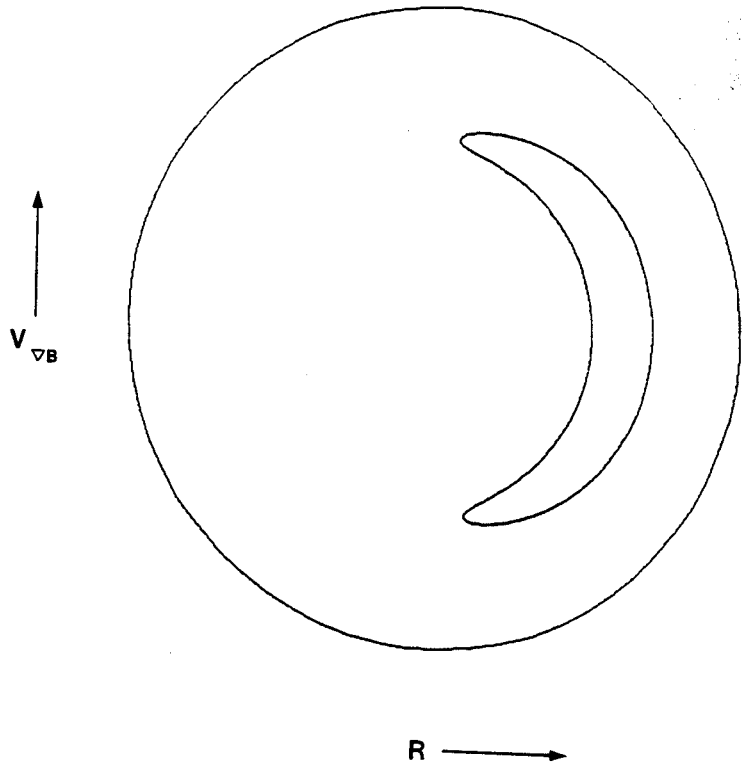

Fig. 12 — Banana orbit with no ripple for a 52.2 keV hydrogen ion. Same plasma conditions as in Figure (11).

IV.2 Integrator

A deferred-limit integrator, called EXTINT, has been written by Boris and Winsor[14]. Based upon the Bulirsch-Stoer extrapolation technique, EXTINT is used to integrate the equations of motion. It has the capability of integrating up to 20 simultaneous first order ordinary differential equations by repeated extrapolation on a midpoint rule. An error subroutine is called after each integration to ensure that the integrated variables are within the tolerance specified by the operator. If the integration is not accurate enough, the step size is halved and the process is repeated. The one drawback of EXTINT is that when accuracy of 10^{-3} to 10^{-5} is needed it will require more extrapolations, and therefore more time, than others methods such as Runge-Kutta, or a multiple-step (i.e., predictor corrector), method. However, the reason that EXTINT has been chosen is that, for a majority of the time, the equations of motion must be integrated to an accuracy of 10^{-5} or greater. In this range, EXTINT is faster than methods mentioned previously and will increase the efficiency of integration. For a more detailed discussion of the particular advantages and disadvantages of EXTINT over other integration schemes, the reader is referred to the paper by Boris and Winsor.

To test the integration scheme and to ensure that there are no coding errors, a plotting routine was attached to the program so that step by step analysis of an orbit is possible. The initial testing of the routine was completed by comparing calculated orbits to published ones. In his doctoral thesis, Goldston[15], has many plots of pinching orbits, circulating orbits, banana orbits, and other strange shapes for ATC parameters. Implementation of ATC parameters into the computer code generated orbits exactly like those published. Further tests were performed by using Alcator C parameters, generating banana orbits, and then comparing their widths with theoretical predictions. Again the agreement was good. All the tests so far have been done with a fixed time step of 300 *ns* and an error criterion (convergence condition) of 10^{-6}. The ability to duplicate ATC orbits and Alcator banana orbits lends confidence to the fact that the integration routine is operating correctly.

IV.3 Scattering

Scattering is treated in energy and pitch angle using the same method as Boozer and Kuo-Petravic[16]. The pitch angle changes from λ_o to λ_n after a time τ by

$$\lambda_n = \lambda_o(1-\nu_d\tau) \pm \left[(1-\lambda_o)^2\nu_d\tau\right]^{1/2}. \tag{25}$$

In this formula ν_d is the deflection collision frequency for ions on ions given by

$$\nu_d = \frac{3}{2}\left(\frac{\pi}{2}\right)^{1/2}\nu_B\frac{\phi(x)-\psi(x)}{x^3}, \tag{26}$$

with ν_B being the Braginskii collision frequency, $\phi(x)$ is the error function,

$$x = \frac{v}{(2T/m)^{1/2}}, \tag{27}$$

and

$$\psi(x) = \frac{\phi - x\phi'}{2x^2}. \tag{28}$$

The energy changes from E_o to E_n after a time step τ by

$$E_n = E_o - (2\nu_E\tau)\left[E_o - \left(\frac{3}{2} + \frac{E}{\nu_E}\frac{d\nu_E}{dE}\right)T\right] \pm 2[TE_o\nu_E\tau]^{1/2}. \tag{29}$$

In this formula ν_E is the energy scattering frequency for ions scattering on ions given by

$$\nu_E = 3\left(\frac{\pi}{2}\right)^{1/2}\nu_B\left[\frac{\psi(x)}{x}\right]. \tag{30}$$

Boozer and Kuo-Petravic write the $\pm$ sign to indicate that the sign is to be chosen randomly, with either sign equally probable. I have chosen to handle this in a different manner. Instead of picking the sign randomly, I have decided to create a normal distribution with the required standard deviation and pick randomly from this distribution. This technique is used for both energy and pitch angle scattering. For example the standard

deviation of the energy scattering is

$$\sigma = 2[TE_o\nu_{ET}\tau]^{1/2}. \tag{31}$$

This method allows you to pick from the entire distribution and not always just one standard deviation from the mean.

Physically, the terms in the pitch angle and energy operators are easy to understand. In the pitch angle equation, the first term tries to drive the pitch angle to the average value which is zero. The second term can be considered to be the spreading away from the average. The pitch angle operator was tested by having a test particle scatter for 1×10^6 events and then plotting the resulting distribution. Figure (13) is a plot of the pitch angle distribution. As can be seen, the results give an equal probability for all pitch angles as is expected.

The second term in the energy operator can be considered to be the drag term. At high energies, the bracket term is positive and the net result is to push the energy down to the thermal region. At very low energies, the bracket term becomes negative with the net result of adding to the energy and driving it toward thermal energies again. This term, like the corresponding pitch angle term, tends to drive the particle to its average value. The third term in the energy operator is the energy scattering term. It provides for the spreading of the energy about the mean as did the corresponding pitch angle term. The energy operator was tested by again letting a test particle scatter for 1×10^6 events and then plotting the resulting distribution. As can be seen by Figure (14), the distribution is a very good representation of a Maxwellian. The only difficulty is in the high energy region near 10 keV where the statistics become poor. Because the operator represents a Maxwellian so well, it is believed to be operating correctly.

IV.4 Numerical computation methods

To enable a calculation of distribution functions, the scattering routine was added to

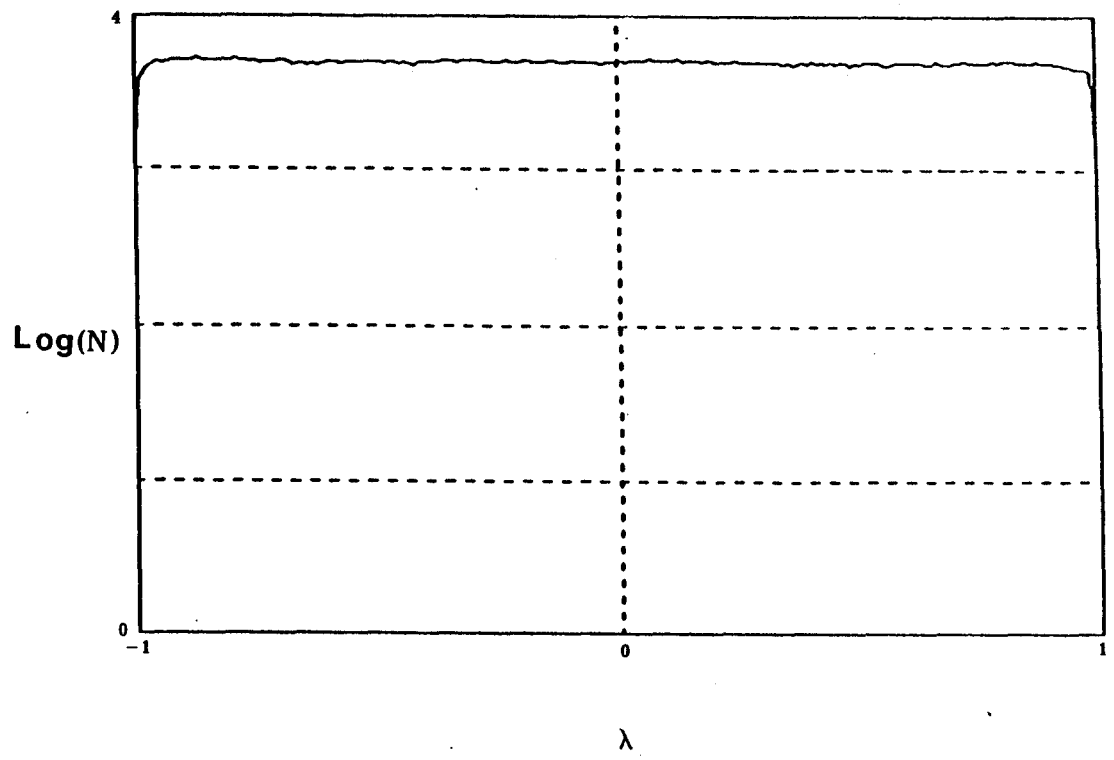

Fig. 13 — Pitch angle distribution generated by a test particle of initial energy 940 eV having one million scattering events against a background Maxwellian of 1.2 keV. N is the number of times a particle entered a given energy bin.

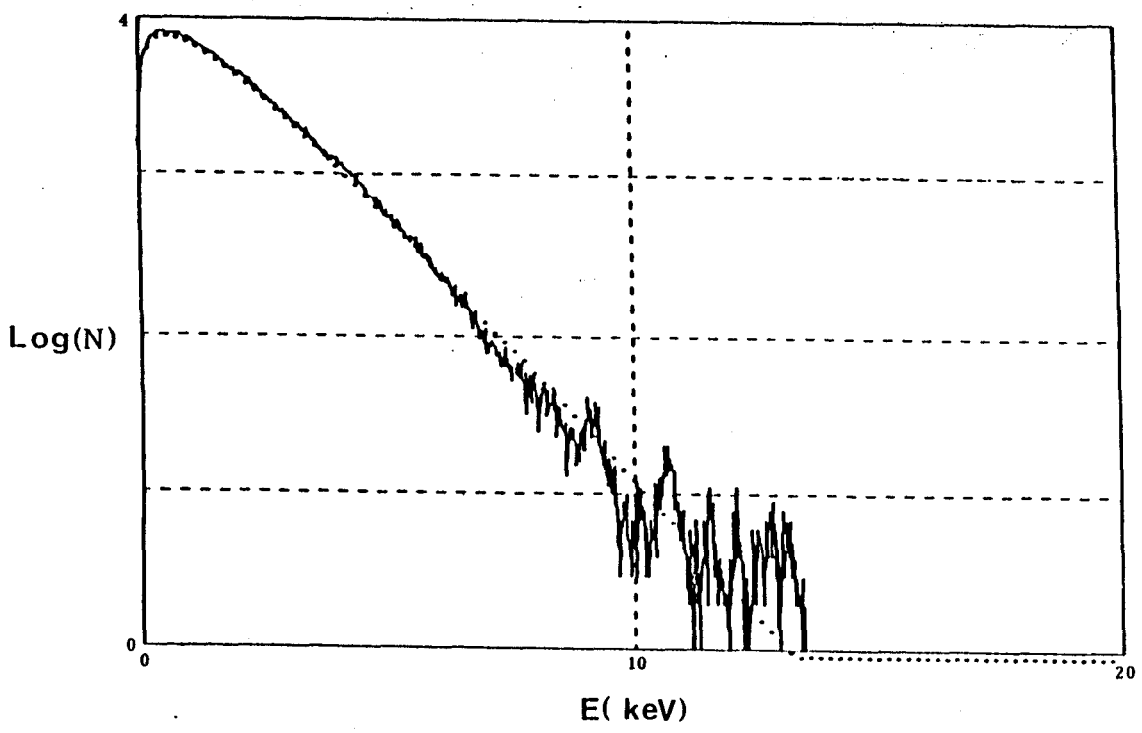

Fig. 14 — Energy distribution generated by the same test particle as in Figure (13).

the existing code, and the graphic routines were removed. Distribution function updating is done after every integration. Modifications have been done to allow for variable time steps and variable error conditions in order to speed up the running time of the code.

The integrator EXTINT has the capability to return what it considers to be the most efficient time step for integration. Unfortunately, it is not possible to let EXTINT independently choose the time step because the scattering condition

$$\nu_d \tau_{int} \ll 1, \tag{32}$$

and

$$\nu_E \tau_{int} \ll 1 \tag{33}$$

must also be satisfied. At high energies, the integration time is determined by the particle's energy, while at low energies, the integration time is determined by the scattering conditions. Furthermore, the larger $\Delta\mu/\mu$ becomes after a scattering event, the greater the tolerable error in the integration (up to some specified limit). With these ideas in mind, the following algorithm has been developed. An initial time step of $300ns$ and an error criterion (convergence condition) of 10^{-6} are chosen. These values are low enough so that all necessary criteria are satisfied regardless of particle energy. EXTINT then integrates the equations of motion and returns the most efficient integration time for the particle just integrated. With the ion at the new position, it is scattered in pitch angle and energy. At this point, the time EXTINT returns is checked against the scattering conditions set forth in the previous two equations. If the time has gotten too large, the integration time becomes either

$$\tau_{int} = \frac{.1}{\nu_d} \tag{34}$$

or

$$\tau_{int} = \frac{.1}{\nu_E}, \tag{35}$$

whichever is smaller. Here, the inequalities of equations (32) and (33) are made equalities by assuming that $.1 \ll 1$ thus satisfying the scattering conditions. Next $\Delta\mu/\mu$ is considered. Instead of calculating $\Delta\mu/\mu$ directly, it is calculated indirectly by comparing the 90^o scattering time to the integration time. As the ratio τ_{int}/τ_{90} approaches 1, so will the ratio $\Delta\mu/\mu$. Since careful monitoring of τ_{int}/τ_{90} will guarantee that the error in μ is always within tolerance, the error allowed in μ is set to be τ_{int}/τ_{90} with a maximum of 10^{-4}. Initially, the error in the four integration variables was set to be equal to the error in μ. However, this increased the run time of the code significantly. At this time, several runs were made with various fractional values of the μ error conditions used for the error conditions of the four integration variables. It was found that 20% of the μ error condition gave accurate answers but did not slow down the integration by an appreciable amount. With these new conditions, the process starts again. All computer runs are started by randomly picking a particle from a Maxwellian in energy, and from a flat distribution in pitch angle. The particle's initial position is picked randomly for $0 \leq \theta \leq \pi$, $0 \leq \phi \leq 2\pi$, and for $0 \leq r \leq a/2$. For diagnostic purposes, the temperature of the plasma is assumed to be uniform over a cross section. This aids in debugging the code. Once things are believed to be in good working order, it is an easy matter to have the temperature vary like

$$T = T_o e^{-r^2/a_T^2} \tag{36}$$

with

$$a_T^2 = \frac{3}{2}\frac{q_0}{q_l}a^2. \tag{37}$$

Equations (36) and (37) are derived from fitting a gaussian to electron temperature profiles measured by cyclotron emission[17]for many values of magnetic field, plasma current, and density. This initial particle is followed until the specified number of integration steps has occurred, or until the particle is lost outside of the limiter radius. If the particle is lost, a new one is picked using the same method as that for the initial particle.

In order to calculate distribution functions, the energy and pitch angle spectra were

divided into 1000 bins between 0 and 20 keV and between —1 and 1 respectively. Once the change to variable time steps was made, each integration should not contribute equally in weight to updating a bin. Instead, bins are weighted by the integration time required.

Loss cones have also been calculated with this Monte Carlo code. When this calculation is done particles are no longer picked randomly. Instead, a grid is set up in velocity space such that there are 25 evenly spaced $v_\perp$ velocities between 0 and $2.5 \times 10^8 cm/s$, and 52 $v_\parallel$ velocities between -2.5×10^8 and $2.5 \times 10^8 cm/s$. The point (0, 0) is not considered. A particle is followed for some multiple of a banana bounce time. A data array makes note of whether the particle was confined or lost in the specified amount of time. With this information, a plot in velocity space can be made to illustrate any loss regions. This illustration is done by blackening in a region where a particle is lost. It should be noted that these loss cone plots are made for a specific region in physical space. Thus many plots are needed to map out the losses in velocity space for Alcator.

IV.5 Computational results

The first distribution function was calculated globally, with the ripple field nulled out. This should generate a Maxwellian distribution in energy and a flat distribution in pitch angle as was done when just the scattering routine was being tested. Figures (15) and (16) are plots of the results, and they are exactly what is expected. Note that this is why the assumption of constant temperature is made. If the temperature had varied, the resulting global distribution would be a sum of Maxwellians, not a single Maxwellian, making diagnostic work more difficult.

Next, the ripple was turned on, and the code was run again. Results of this second run are shown in Figures (17), (18), and (19). The energy distribution seen here is noticeably different than that in Figure (15). Figure (17) shows a distribution which is Maxwellian to 8.5 keV and then starts to deplete until 11 keV where it drops down to nill. No conclusion can be drawn from the sharp cutoff of the distribution because the effect is too far down the

statistical noise. The curious aspect of this computer run is illustrated in Figure (19). The particles which are lost are all of energy below 6.5 keV, yet the derived energy spectrum shows no depletion up to 8.5 keV. Furthermore, the experimental spectrum shown in Figure (1) is depleted at energies above 8 keV. The question to be addressed is why are the particles being lost at low energies instead of at higher energies where the depletion is observed.

A further investigation of the scattering operator used in the code will allow us to understand why the lost particles are of low energy. Figures (20) and (21) are plots of energy versus time and of pitch angle versus time for a particle of initial energy 43 keV which scatters to thermal energies. These plots are generated just from the scattering operator. There is no integration of the equations of motion. Immediately obvious is, that at high energy, the particle's pitch angle does not change by much. As the particle's energy begins to decrease, the change in pitch angle is still small until it reaches several T_i, and the pitch angle begins to change dramatically. This suggests that, as particles scatter from thermal to higher energies, they will form "probability lobes" which look like mouse ears that are fat at the thermal energies and become slimmer as energy is increased. Figure (22) is a series of graphs which show a particle at energy 20 keV thermalizing from different positions in velocity space. If lines are drawn around the maximum pitch angle excursion, "probability lobes" are created just as described. Figure (23) is a series of plots showing a particle starting at T_i and jumping up ion energy. The same effect is seen. A particle makes a small energy excursion with a very limited pitch angle range. Stated simply, particles of higher energy pitch angle scatter less than particles of lower energy.

Now imagine a loss cone in velocity space with its lowest point at 5 keV. Particles will not pitch angle scatter into the loss cone at high energies, except for those few right next to the loss boundary. Instead, the only way they may enter the loss cone is by scattering up in energy toward the loss cone. To test this hypothesis, the program which was used to create Figures (22) and (23) has been modified. A loss boundary in velocity space is simulated by the equation for a hyperbola

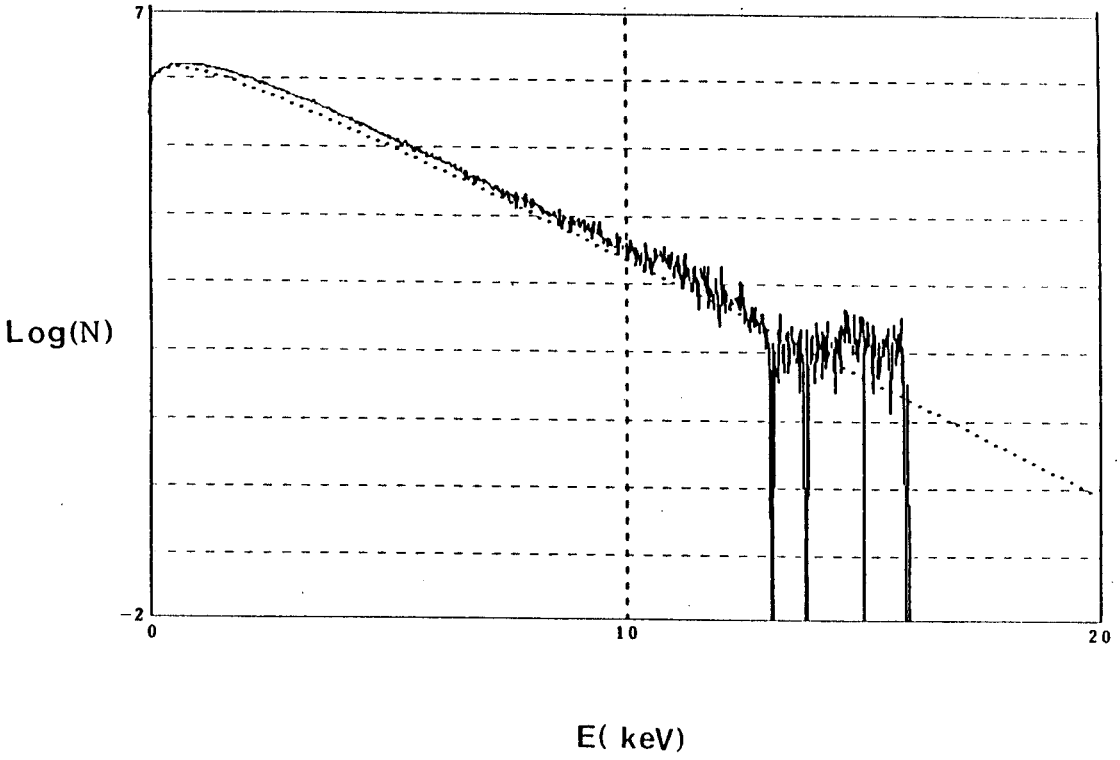

Fig. 15 — Global energy distribution for hydrogen after one million scattering events with no ripple. $B_T = 8\,T, q_l = 4, q_o = .9, a = 17\,cm, T_i = 1200\,eV, n_e = 5 \times 10^{14}\,cm^{-3}$. N is the time weighted number of particles in a given energy bin.

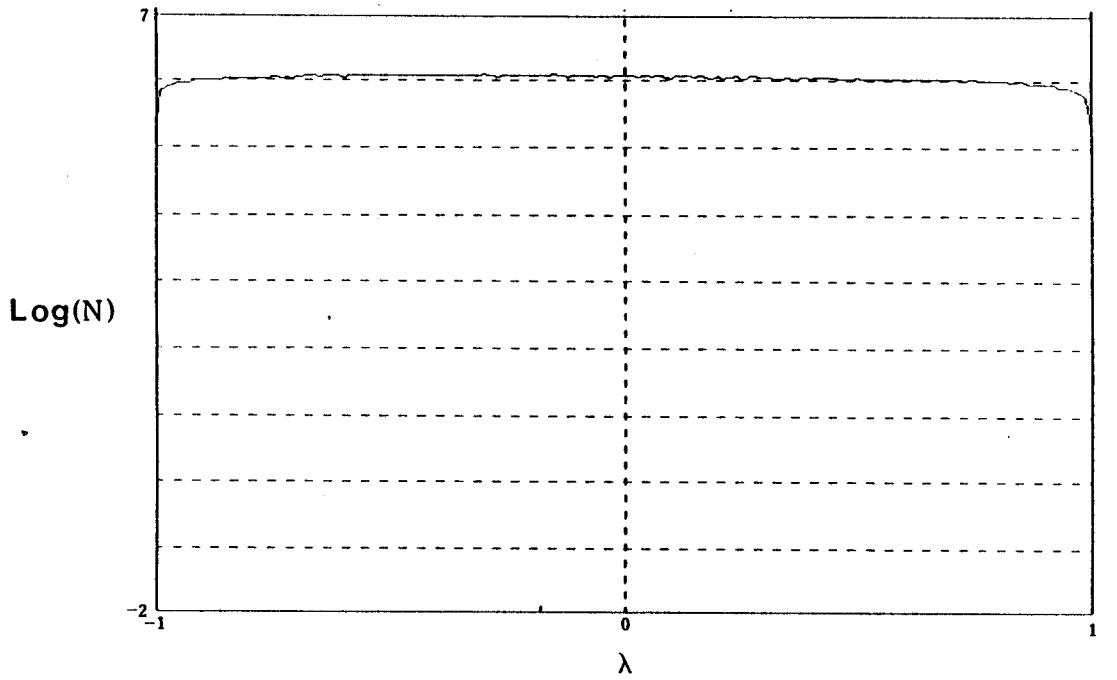

Fig. 16 — Pitch angle distribution with no ripple. Generated from the same data as in Figure (15).

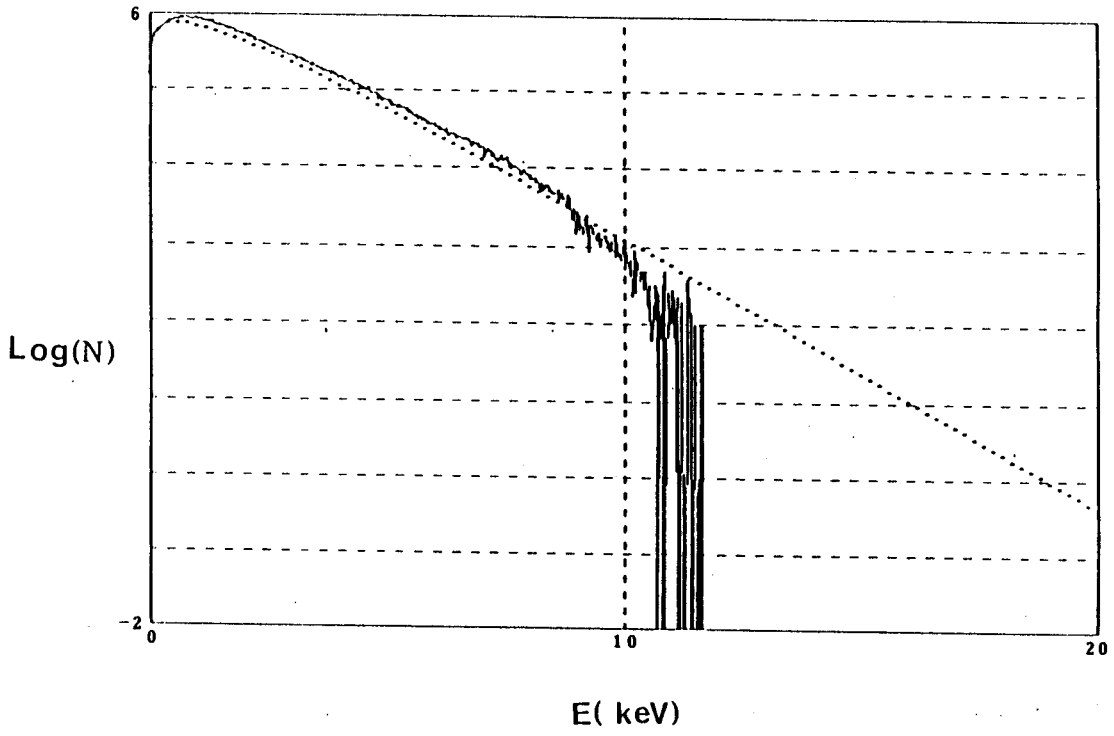

Fig. 17 — Global energy distribution for hydrogen after one million scattering events with standard Alcator ripple. Same plasma conditions as in Figure (15).

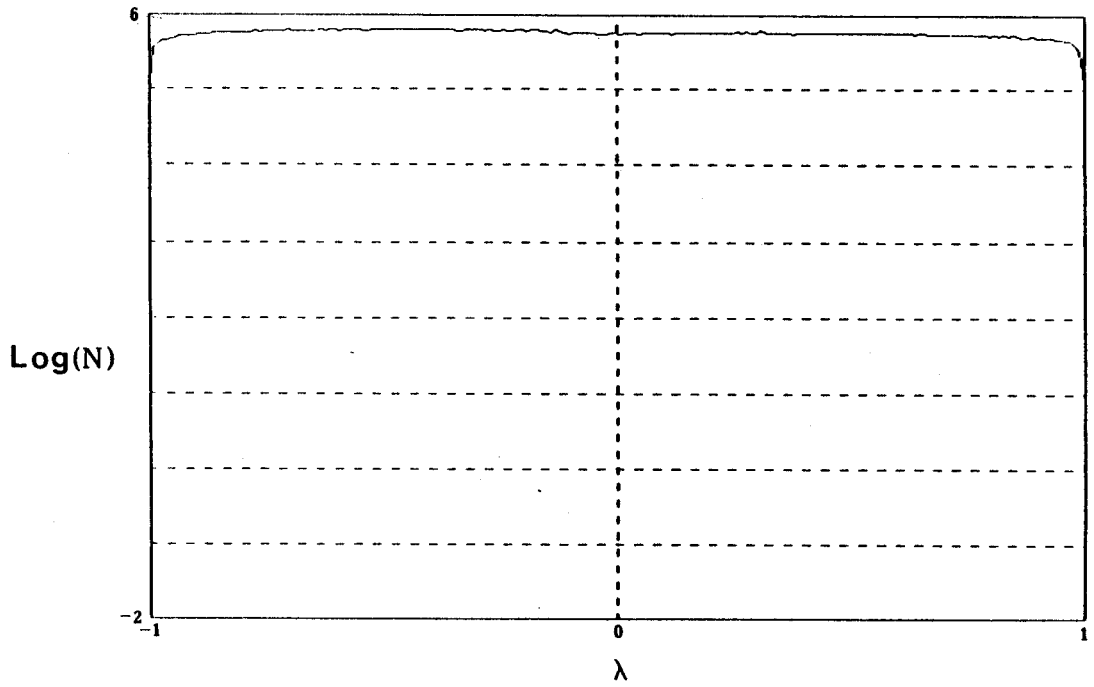

Fig. 18 — Pitch angle distribution with standard Alcator ripple. Generated from the same data as in Figure (17).

$$\left(v_{\perp}^{*}\right)^{2} = v_{\perp}^{2} - Av_{\parallel}^{2}. \tag{38}$$

Here $v_{\perp}^{*}$ is the velocity on the $v_{\perp}$ axis corresponding to 5 keV, and the A is used to simulate the correct angle of the loss cone. When a particle crosses this boundary, it is assumed lost, its position in velocity space is recorded, and a new particle is started. After many particles are considered, a plot is made by placing a dot where each particle is lost. If it is true that particles are lost at lower energies, this plot should have a high concentration of dots near the low end of the cone. Figure (24) is a plot of the results, and they are exactly as expected. The majority of particles will not pitch angle scatter into the loss cone.

It is important to understand if the effect illustrated in Figures (20) and (21) is an accurate representation of coulomb collisions. Scattering is governed by three equations. The slowing down, or energy drag, term is

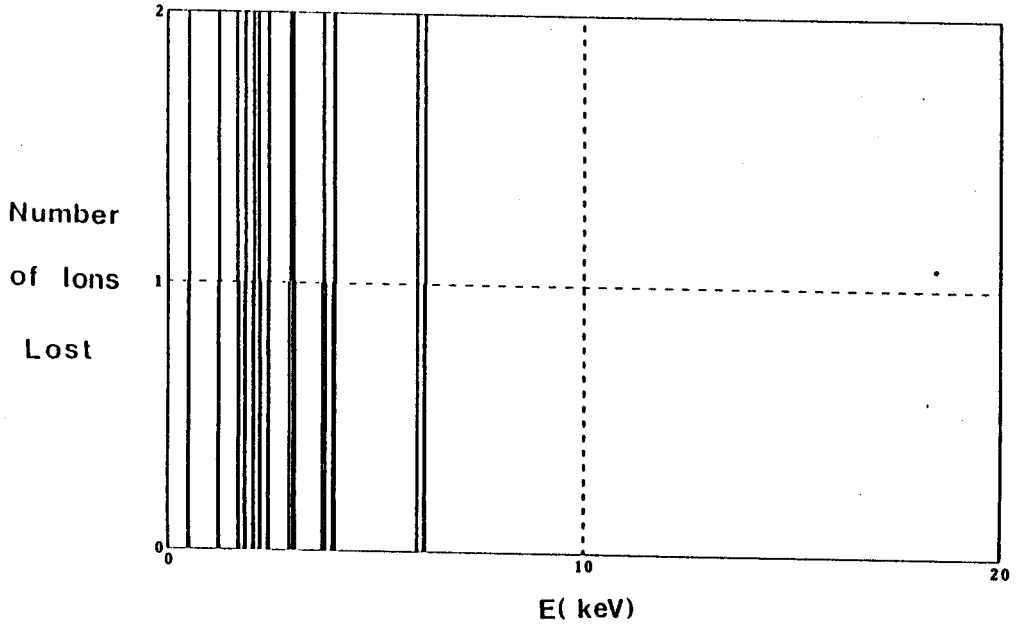

Fig. 19 — Histogram of depleted particles. Generated from the same data as in Figure (17).

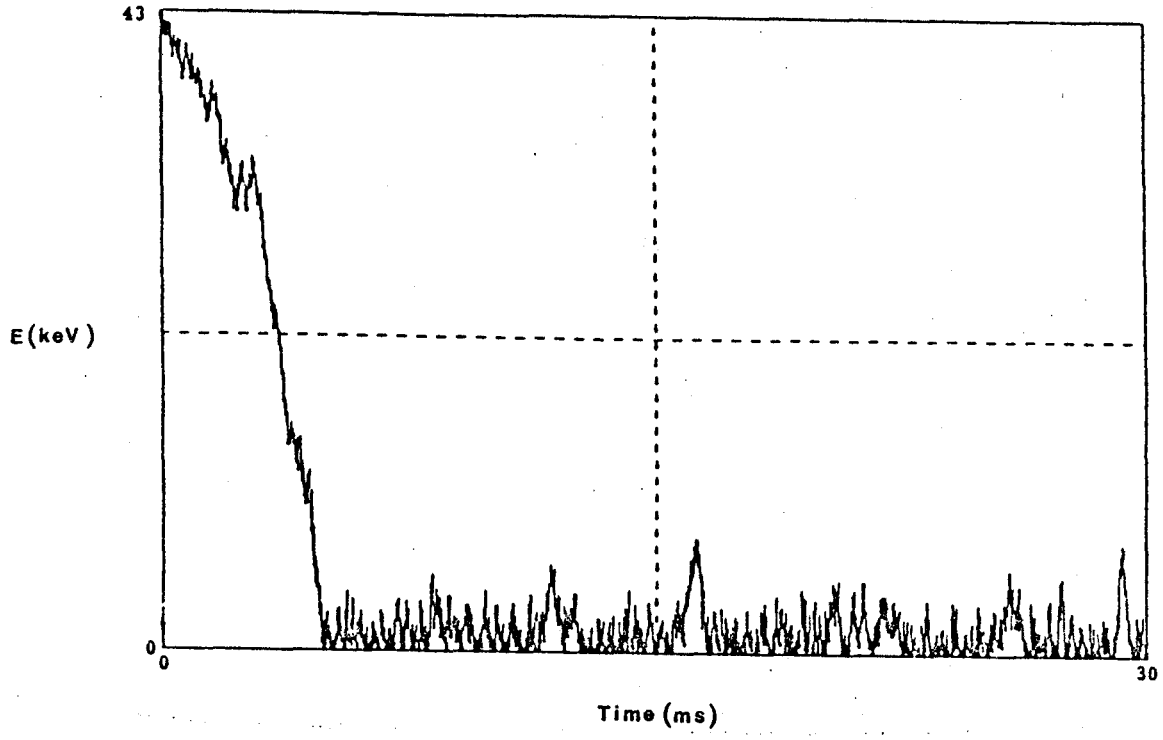

Fig. 20 — Change in ion energy versus time due to scattering against a background Maxwellian of 1.2 keV.

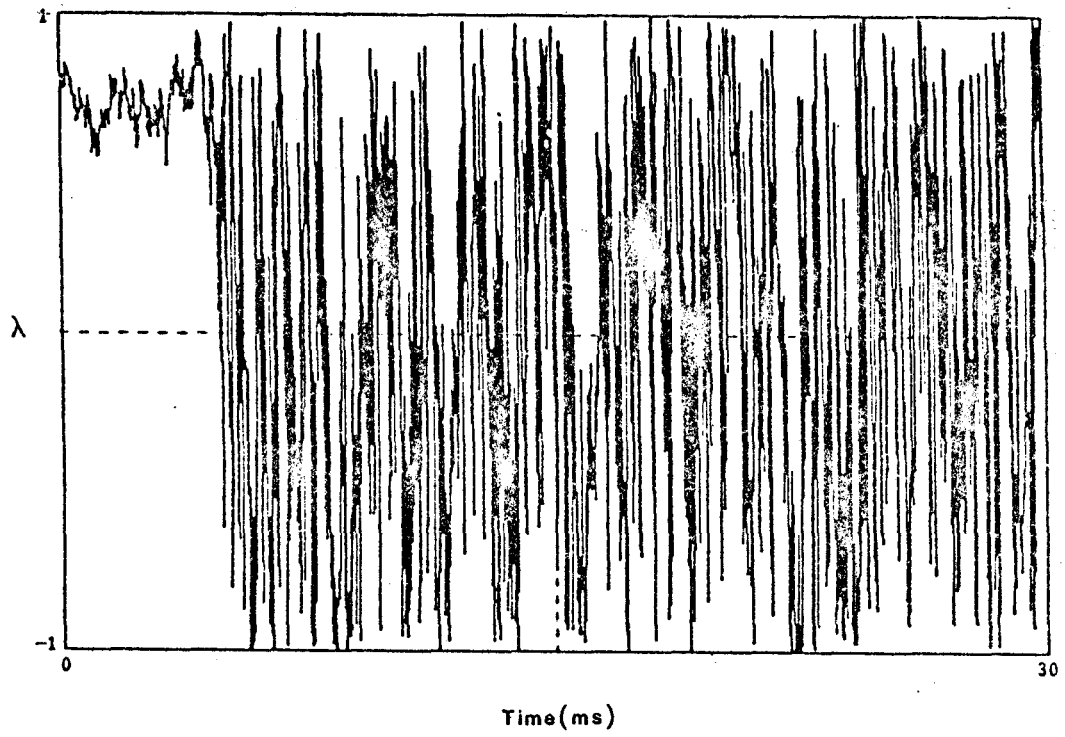

Fig. 21 — Change in ion pitch angle versus time due to scattering. From the data as in Figure (20).

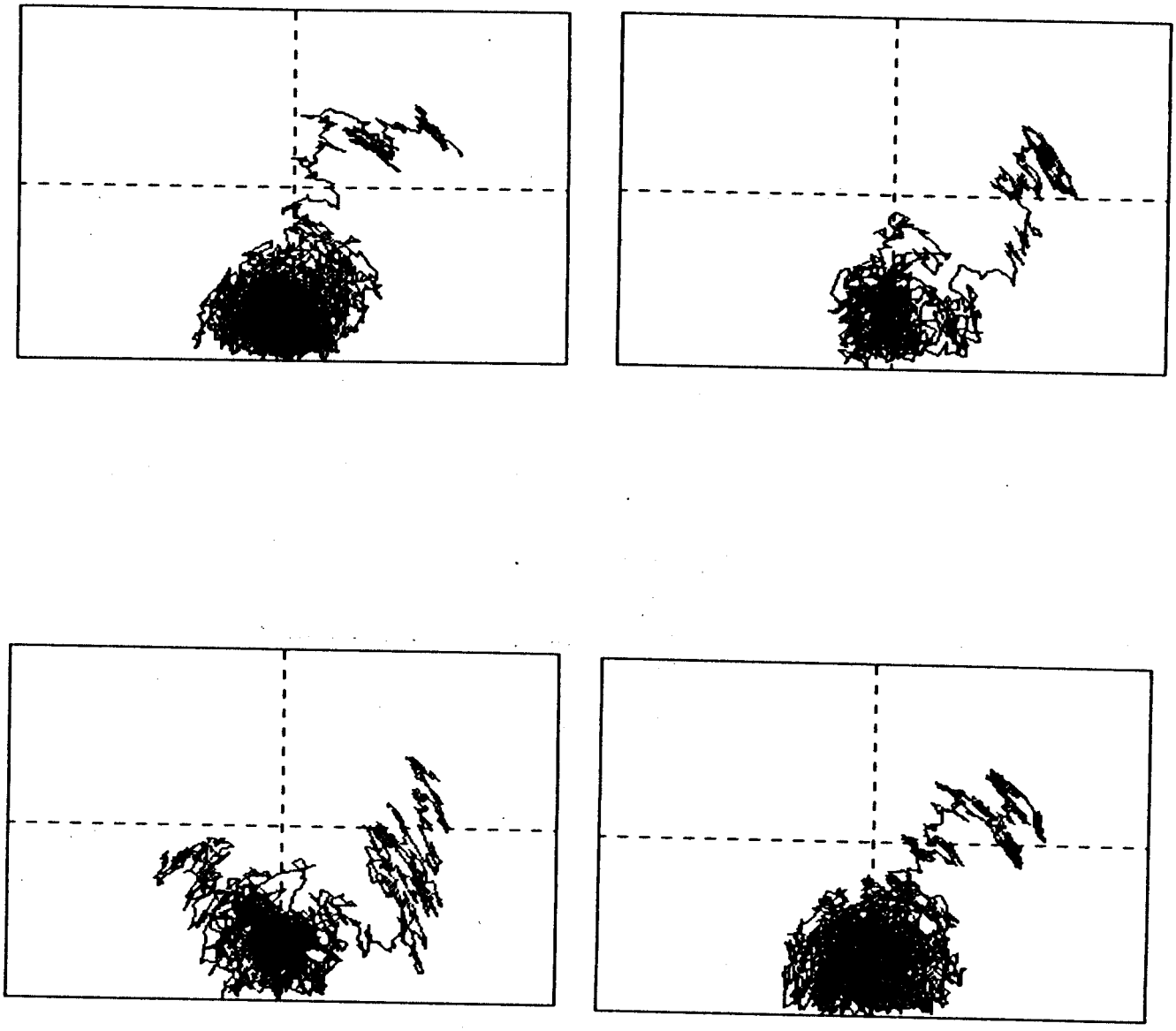

Fig. 22 — Shown here are several hydrogen ions of initial energy 20 keV scattering against a background Maxwellian of 1.2 keV. The vertical axes are $V_\perp/V_o$ from 0 to 2.55. The horizontal axes are $V_\parallel/V_o$ from -2.55 to 2.55. $V_o = 1 \times 10^8\, cm/sec.$

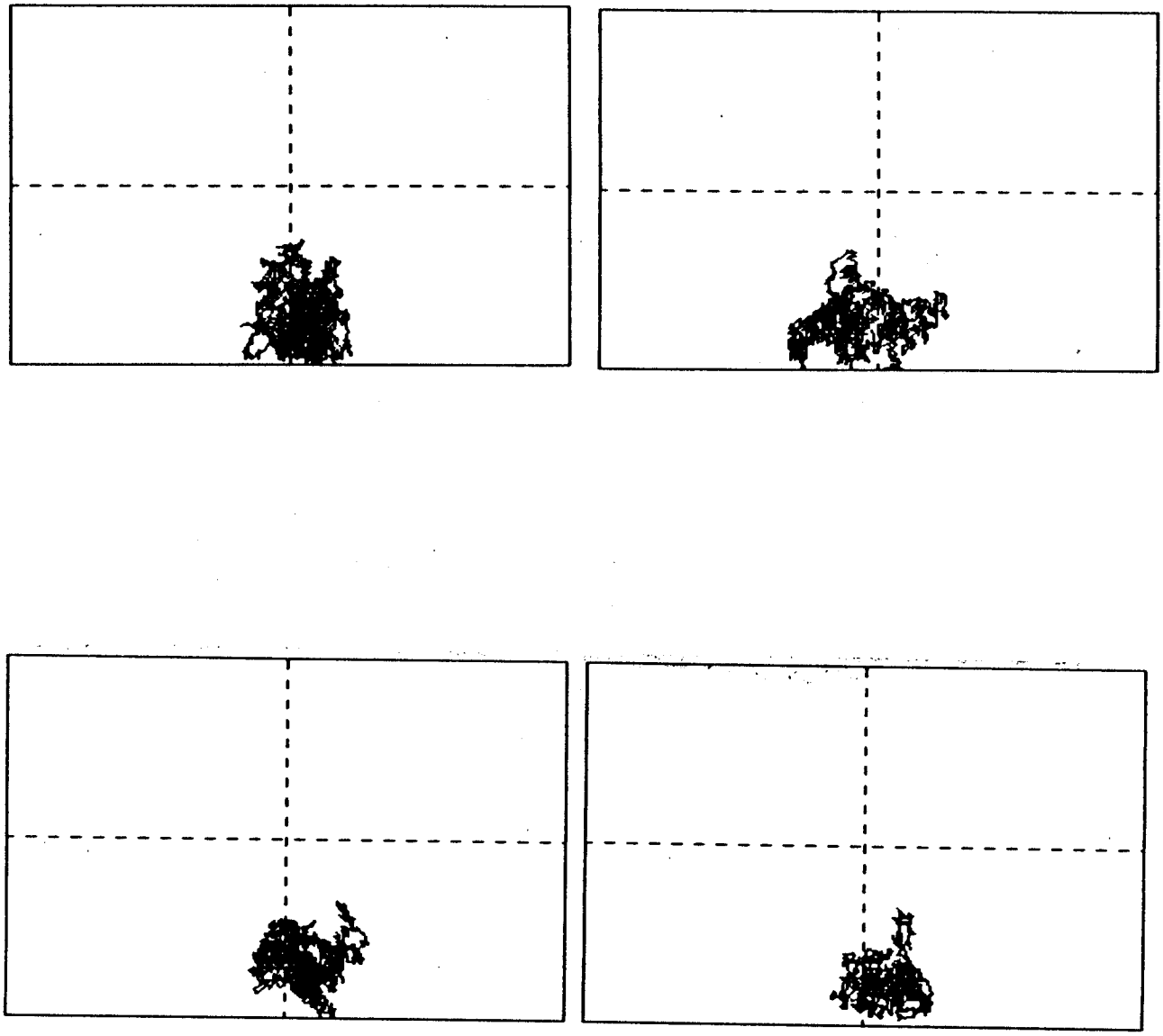

Fig. 23 — Shown here are several hydrogen ions of initial energy 1.2 keV scattering against a background Maxwellian of 1.2 keV. The vertical axes are $V_\perp/V_o$ from 0 to 2.55. The horizontal axes are $V_\parallel/V_o$ from -2.55 to 2.55. $V_o = 1 \times 10^8\, cm/sec.$

$$\frac{dv_\alpha}{dt} = -\nu_s^{\alpha/\beta} v_\alpha. \tag{39}$$

The energy, or parallel, diffusion equation is

$$\frac{d}{dt}(v_\alpha - \bar{v}_\alpha)_\perp = \nu_\perp^{\alpha/\beta} v_\alpha^2, \tag{40}$$

while the pitch angle, or transverse, diffusion equation is

$$\frac{d}{dt}(v_\alpha - \bar{v}_\alpha)_\parallel = \nu_\parallel^{\alpha/\beta} v_\alpha^2. \tag{41}$$

Here, α is the test particle streaming through a background of field particles β. For $\alpha = \beta$ and for fast test particles, $\nu_s \approx \nu_\perp > \nu_\parallel$. Expressing equations (39) and (41) simply in terms of Δv yields

$$\Delta v_\alpha = (\nu_s \tau) v_\alpha, \tag{42}$$

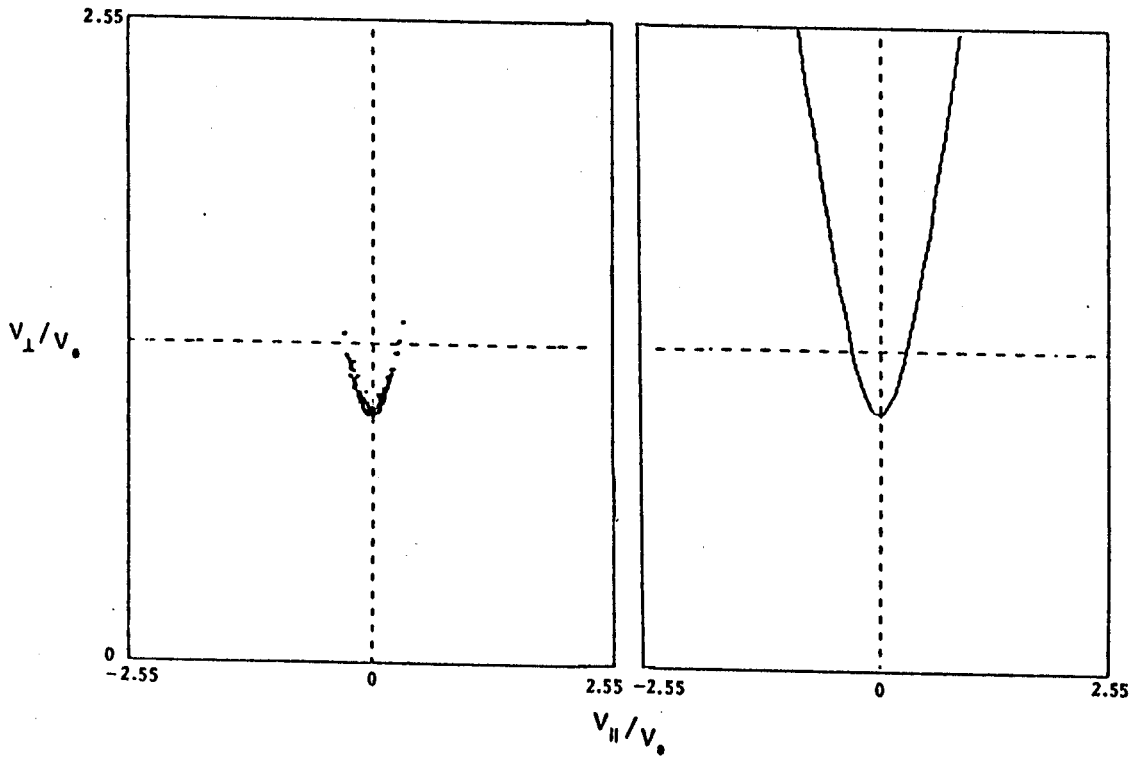

Fig. 24 — Illustration of the points where ions enter the loss cone. The graph on the right is the simulated loss cone. The graph on the left represents where an ion has entered the loss cone. These points are for hydrogen scattering against a Maxwellian of 1.2 keV. $V_o = 1 \times 10^8\ cm/sec.$

and

$$\Delta v_{a\perp} = (\nu_s \tau)^{1/2} v_a. \tag{43}$$

On a short time scale $\nu_s \tau < 1$, the pitch angle diffusion and the energy diffusion are comparable. So on the microscopic level, it is expected that a particle will move over all of velocity space as it changes energy. Unfortunately, this view is too simplified. The pitch angle diffusion term is proportional to $(\nu_s \tau)^{1/2}$. For $\nu_s \tau > 1$, the drag term will begin to dominate. This is just illustrating the difference of the drag term, which is always directed to thermal energy, versus the pitch angle term, which is diffusive. The pitch angle change begins to wash out while the energy change continues down (this is neglecting energy diffusion which at higher energies will play a small role). Therefore on time scales the order of a thermalization time, the energy drag term will dominate over the pitch angle term. An ion thermalizing from high energies will have small pitch angle excursions. Similarly, an ion which scatters up to high energies (those cases where the energy diffusion term is enough to counteract the drag) will have to do so quickly because the longer it waits, the better chance the drag has of winning out and pulling the particle down to thermal energies. In the short time it takes the particle to jump to high energy, it will have a very small amount of time to pitch angle scatter an appreciable distance. The implication is that particles will enter the loss cone from low energies, not by pitch angle scattering at high energies. This behavior is exactly that of the scattering model.

The implication of particles entering the loss cone from low energies is clear. There are no particles in the loss cone at high energies, except for those few which lie just on the boundary. Therefore, the charge exchange analyzer, which sees almost exclusively perpendicular particles, should see a distribution which begins to deplete and then has a sharp cutoff. Figure (1) begins to show these characteristics. Unfortunately, the data points above 11 keV are lost in the noise. Furthermore, the global energy distribution of Alcator should be slightly depleted.

The data displayed in Figure (17) required 52 CPU hours to produce on a Digital VAX

11/780. In that time 10^6 scattering events were simulated resulting in 1.1 seconds elapsed of real time. The fact that approximately 2 days of CPU time is necessary to complete one computer run is unfortunate. Basically, 10^6 interactions is just enough to make the statistics acceptable at energies around 10 keV. Once the numerical bins are selectively incremented to calculate localized distribution functions, the statisfics will become even worse. This is indeed the case as can be seen by Figures (25) and (26). These plots are from a run where the numerical bins were incremented only when the particle was physically within any of the six ripple wells. The problem has now begun to shift away from plasma physics and toward numerical methods.

The number of interactions needed to generate good statistics for distribution function calculations are not necessarily needed for loss cone calculations. Thus, some interesting information can most likely be obtained from the code in its present state by doing loss cone calculations. The theory of loss boundaries was handled in good detail by Goldston[15]. Using his technique of analysis, a computer code[18] has been developed to plot loss boundaries in velocity space for Alcator parameters. An initial test was performed by calculating a loss cone with the ripple field nulled out for hydrogen and deuterium at a position of $r/a = .8$, $\theta = 0$, and $\phi = 0$. The only losses which should occur are due to those counter streaming ions which are banana trapped. Comparison of the theoretical curves in Figures (27) and (29) to the computer derived curves in Figures (28) and (30) give an excellent agreement. Theoretically for hydrogen, the lowest energy lost is 10.1 keV. This compares to the Monte Carlo calculation of 9.7 keV. For deuterium, the theoretical and Monte Carlo numbers are 5.1 keV and 5.4 keV respectively. This not only gives us confidence that the loss cone method of analysis is correct but that the main workings of the Monte Carlo code are indeed correct. The next condition to test is adding standard Alcator ripple to the previous test runs. These results are shown in Figures (31) and (32). As can be seen, the ripple loss cone is added on with the expected angle of $\delta B/B \approx 3\%$.

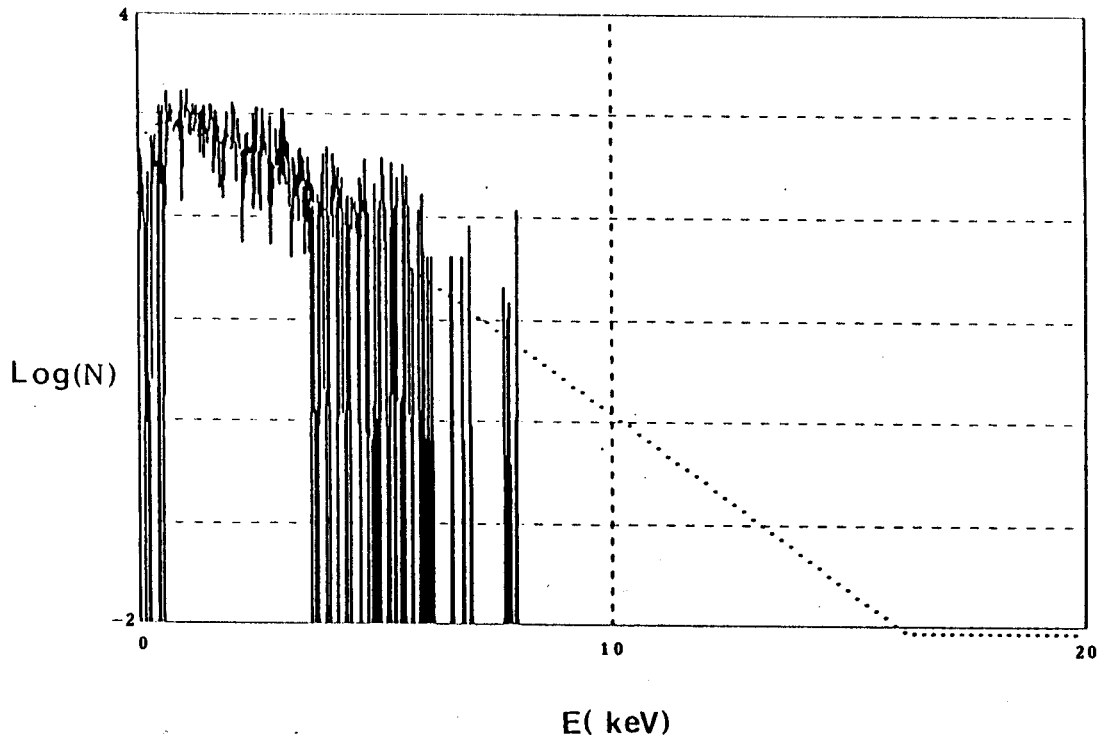

Fig. 25 — Energy distribution in the ripple well. Same plasma conditions as in Figure (15).

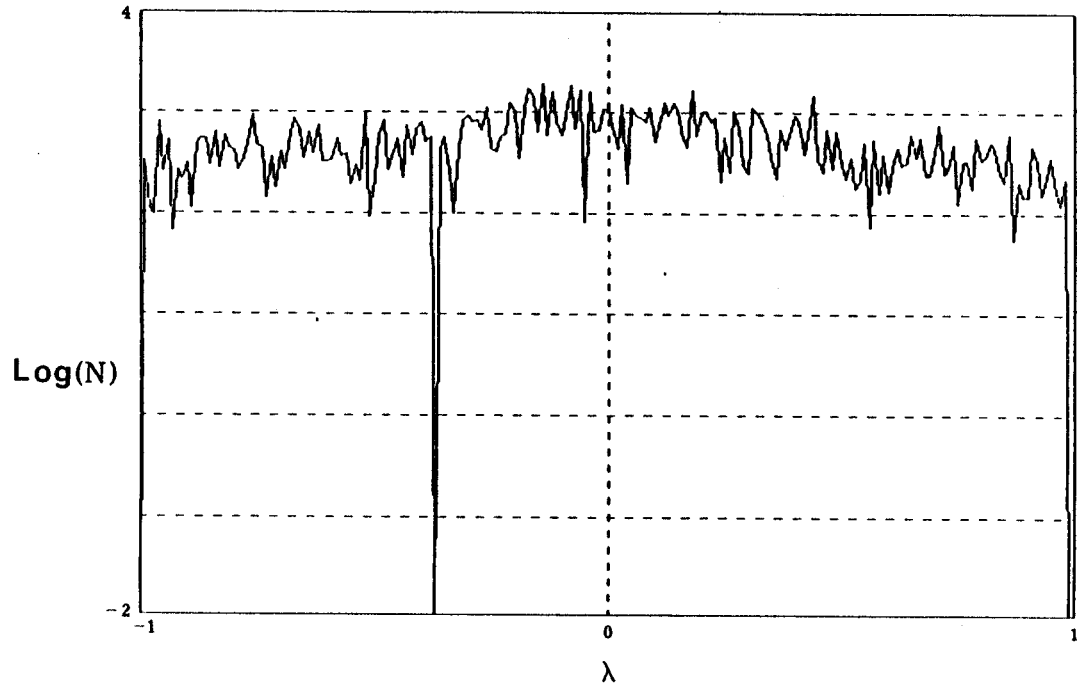

Fig. 26 — Pitch angle distribution in the ripple well. Generated from the same data as in Figure (25).

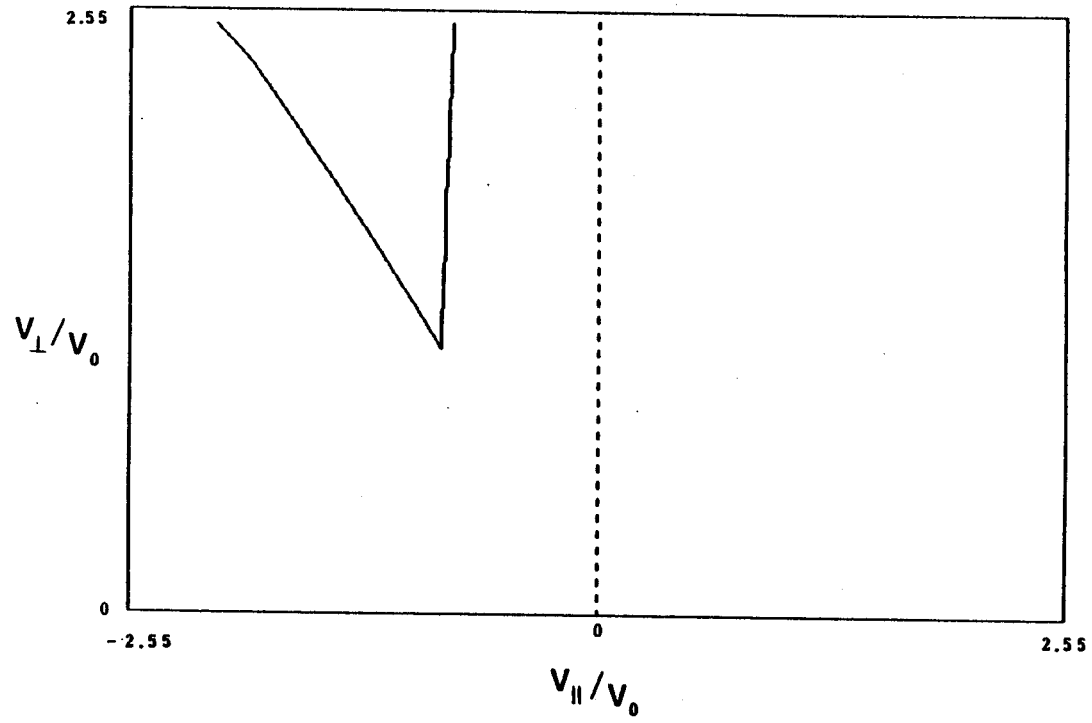

Fig. 27 — Theoretical loss boundaries for hydrogen with no ripple. $B_T = 8\,T$, $q_l = 4$, $q_o = .9$, $a = 17\,cm$, $T_i = 1200$ keV, $n_e = 5.o \times 10^{14}\,cm^{-3}$, $V_o = 1.0 \times 10^8\,cm/sec$.

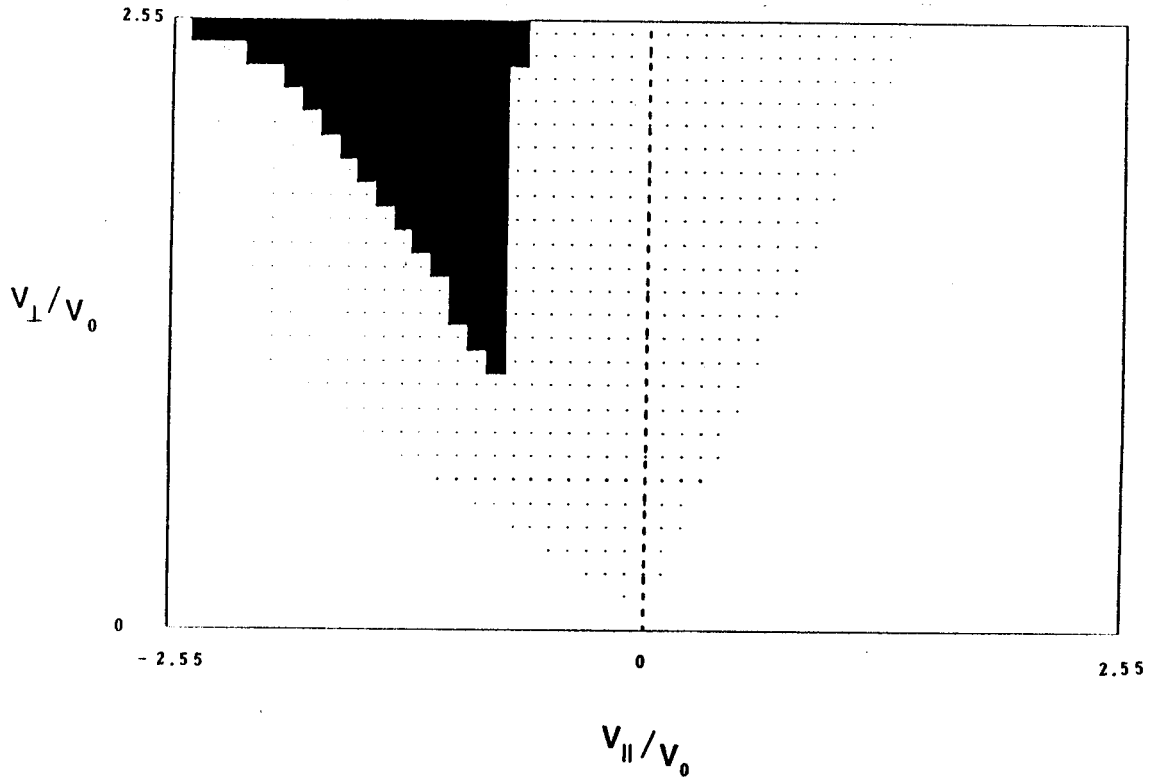

Fig. 28 — Computer derived loss boundaries for hydrogen with no ripple. Same plasma conditions as in Figure (27).

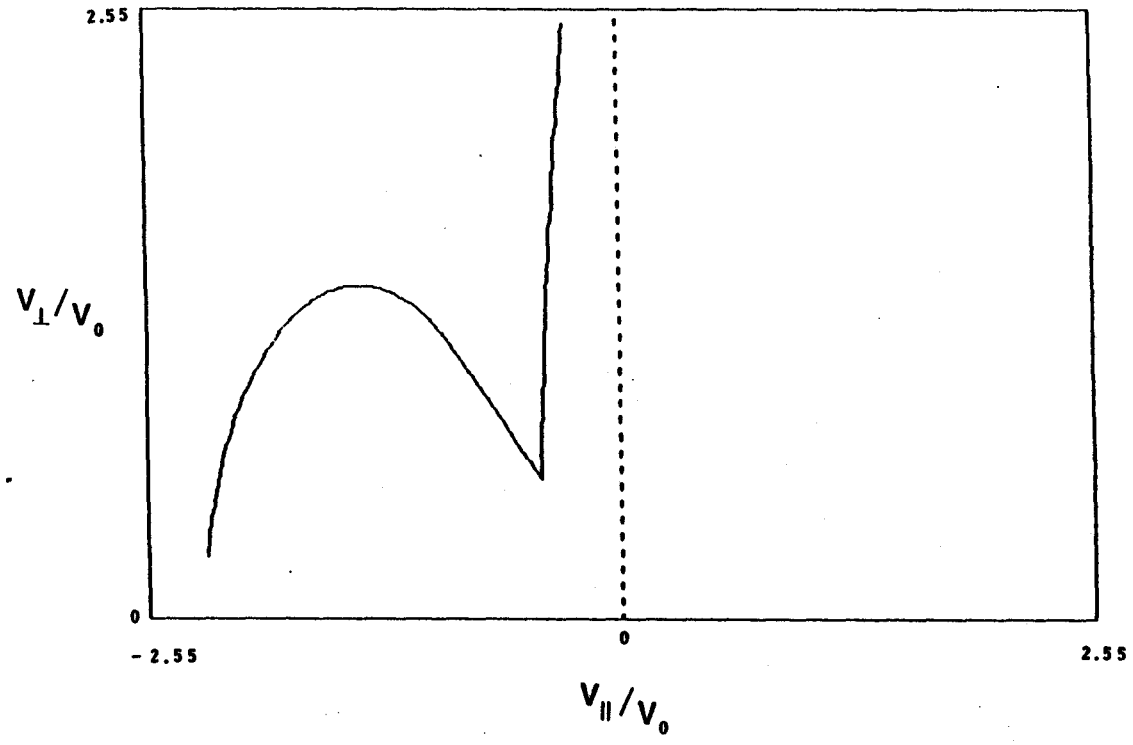

Fig. 29 — Theoretical loss boundaries for deuterium with no ripple. Same plasma conditions as in Figure (27).

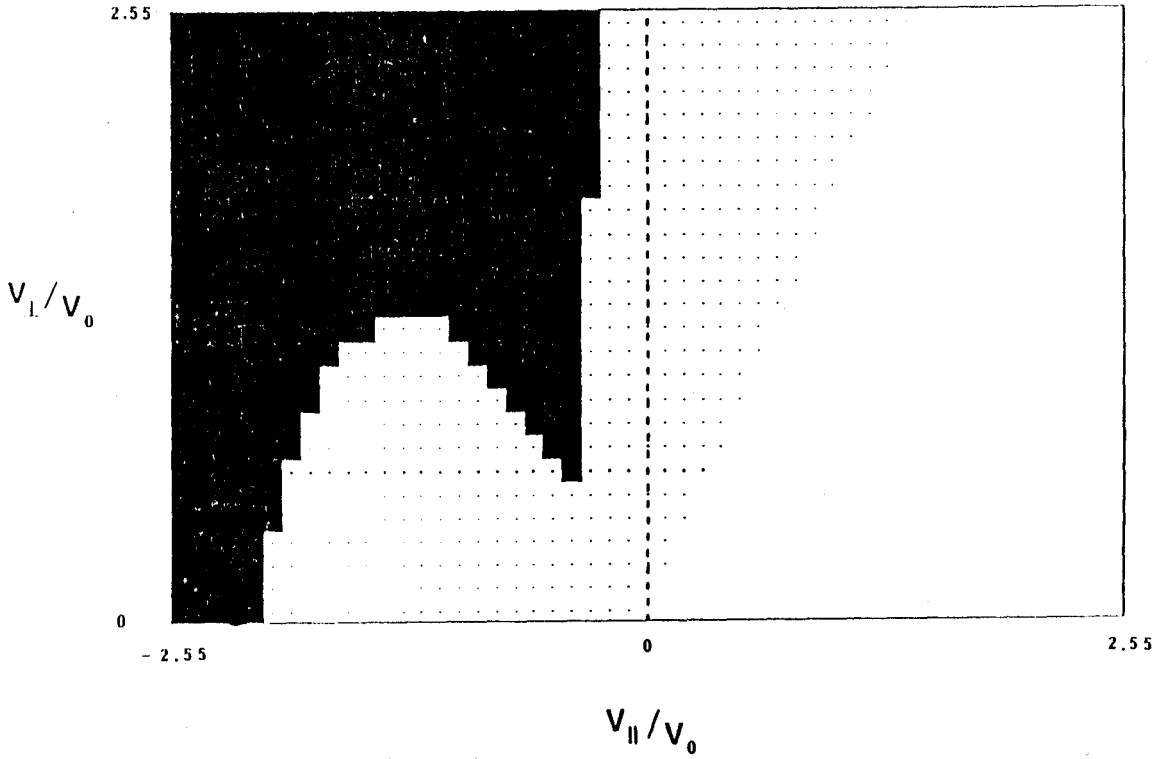

Fig. 30 — Computer derived loss boundaries for deuterium with no ripple. Same plasma conditions as in Figure (27).

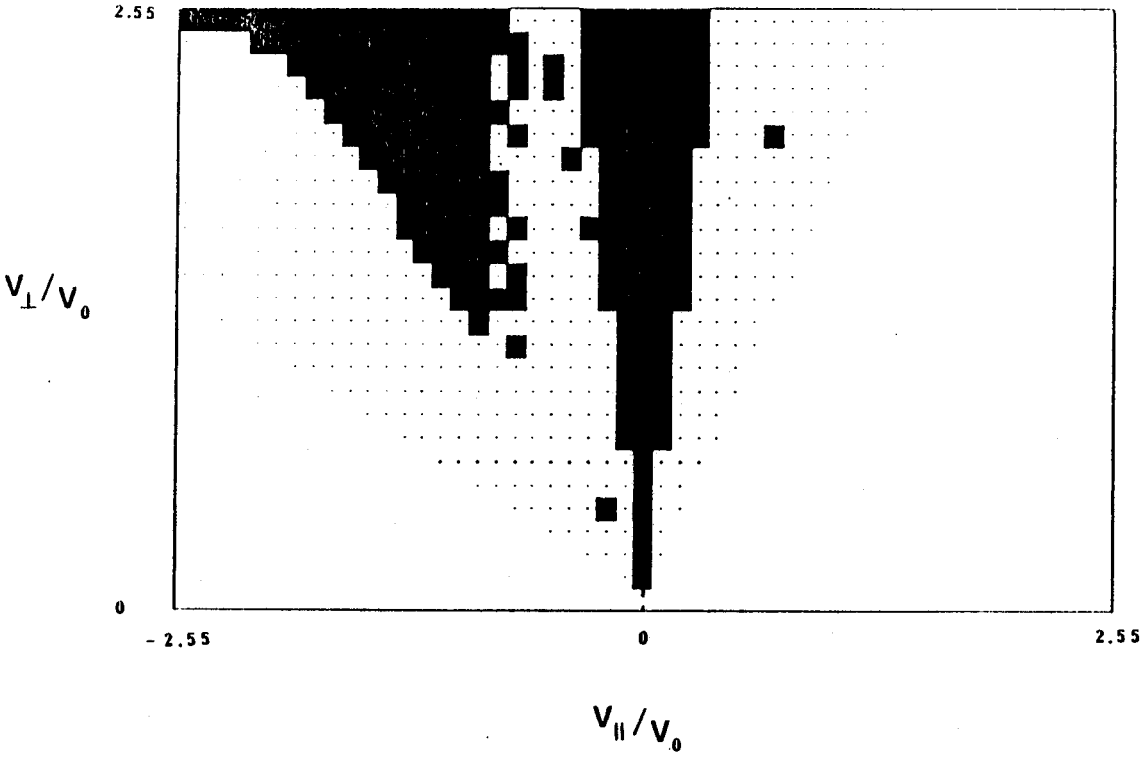

Fig. 31 — Computer derived loss boundaries for hydrogen with standard Alcator ripple. Same plasma conditions as in Figure (27).

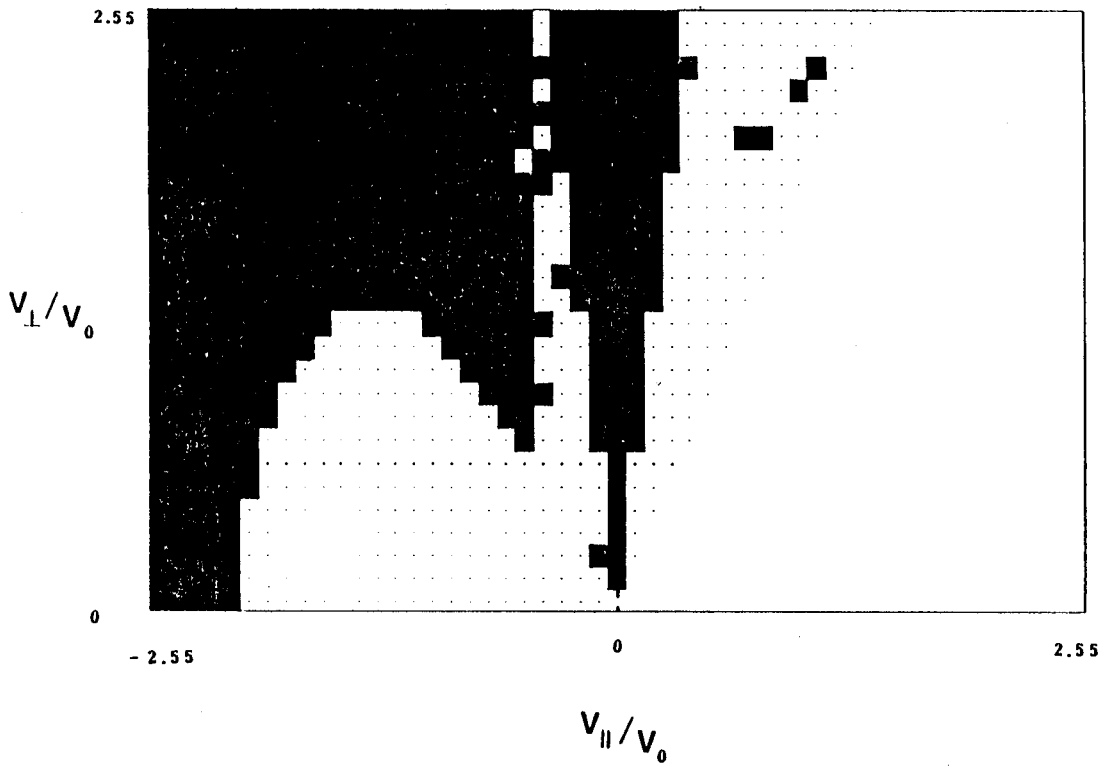

Fig. 32 — Computer derived loss boundaries for deuterium with standard Alcator ripple. Same conditions as in Figure (27).

V SUMMARY AND RECOMMENDATIONS FOR FUTURE WORK

V.1 Principle results

To summarize the work done so far, an accurate analytical model of the magnetic field ripple in Alcator has been created. A scattering operator developed by Boozer and Kuo-Petravic has been adapted for use. This operator,which scatters in energy and pitch angle, has been tested by following a test particle for 10^6 interactions and then observing that the resulting distributions are accurate. Agreement is excellent. This field model, along with a scattering operator, is used in a three dimensional Monte Carlo computer code which tracks the guiding center of an ion. Banana loss boundaries for Alcator have been studied and are in excellent agreement with neoclassical theory. Ripple loss cones have been obtained, and they also agree well with neoclassical theory. These plots confirm that, for deuterium near the edge of a typical Alcator plasma, almost half of velocity space is covered with ions which will eventually become lost. From these results, it is easy to conclude that the ripple of the magnetic field is playing a significant role in particle trajectories.

In order to understand the role ripple plays in ion orbits, an attempt has been made to calculate energy and pitch angle distributions. Global distribution functions have been calculated and show a slight depletion at higher energies. Particles which are ripple trapped and lost are at energies below where depletion is observed. It is found that ions pitch angle scatter less as energy is increased. The result is that, when viewed in velocity space, ions form "probability lobes" the shape of mouse ears which are fat near the thermal energy. Therefore, particles enter the loss cone at low energies near the bottom of the cone. Finally, attempts have been made to calculate distributions which are localized in the ripple well. As of yet, these localized distribution functions have not been calculated due to the extraordinary large amounts of computer time required on a VAX.

V.2 Recommendations for future study

Many tricks have already been attempted to speed up the running time of this code. One method, which was developed decades ago for studying neutron diffusion, is called Splitting and Russian Roulette[19]. This technique is used to improve particle statistics. When used in plasma physics, it is supposed to produce better statistics at higher energies where there are fewer particles. There are no published results for the technique of Splitting and Russian Roulette in regard to particle following in high temperature plasmas. Only a paper by Harvey[20] attempts to address how this technique should be implemented. In the Monte Carlo code presented in this thesis, no success was found with the method of Splitting and Russian Roulette. The problem which was always encountered in this code is the same as others have seen. That is, the sum of the statistical weights of all the particles at the end of a run was considerably less than the weight of the parent particle which started the run. The problem of a non conservation of particles has yet to be resolved.

As far as future ideas are concerned, the most fruitful avenue to take appears to be in vectorizing the Monte Carlo code. In the past, it was believed that Monte Carlo codes did not vectorize very well. But recent work by Brown[21] at the University of Michigan and at Knolls Atomic Power Laboratory indicate that significant decreases in operating time are possible. His work has been performed on Control Data's CYBER-205. Unfortunately, access to this machine is difficult from the MIT Plasma Fusion Center. Instead the CRAY-1S computer, which is a vectorized system and is on the NMFECC link is easy to access from PFC. Estimated time savings by moving from the VAX 11/780 to the CRAY-1S is around a factor of 40. This estimate comes from considering that on the CRAY-1S system an operation plus a memory call takes around 25 ns, while on the VAX computer a similar task will take on the order of 1 ms. Such an increase will allow present global distribution function calculations to be accomplished in merely 1 CPU hour and localized distribution functions in around 10 CPU hours.

Another possible time saving technique would be to store in memory the magnetic field

parameters needed in the equations of motion. Thus, instead of doing repeated calculations at each spatial position, the code would simple "look up" the required values and do a spline fit. There are several drawbacks to spline fitting. The first is that a large quantity of memory is required. This problem can be circumvented by using the CRAY-1S computer which has roughly four times more memory than the VAX. The second problem is machine independent. Unfortunately spline fitting techniques are approximations. If this technique was used on the analytical ripple field model, it would mean approximating an approximation. Instead, if a spline technique is used, it makes more sense to model the currents which are generating the fields. The resulting fields can be represented to any accuracy desired and may be fit together by splines. When work was started on this Monte Carlo code, it was decided to try to use an analytical field model so that both speed and accuracy could be guaranteed. By using the spline technique, it is quite possible that speed could be lost in order to guarantee the same accuracy. Certainly, if this method is tried, a comparison between the analytical method and the spline method must be made. In this comparison, the question of whether the sacrifice of accuracy is worth the increase in efficiency must be addressed.

Once the problem of operating time has been solved, there are numerous plasma physics issues to be examined. The issues mentioned in the beginning of this work, such as depletion of the Charge Exchange spectrum and ripple loss rates on plasma heating schemes, must still be answered. Also, additional questions have been raised during the course of study. The most prominent of those lies in the creation of the analytical magnetic field ripple model. Large amounts of time were spent creating a vector potential representation of B_{rip} to insure a divergence free system. At the present time, many Monte Carlo particle following codes used throughout the fusion community do not have divergence free fields. It would be very interesting to investigate the effect of a non divergence free field on particle orbits. If it is found not to be too crucial, then it is quite possible to represent B_{rip} directly and even more accurately. If it is found to be crucial to have $\nabla \cdot \boldsymbol{B} = 0$, then work can begin on improving the present vector potential model. The two main characteristics which

should be introduced are the off-center nature of the ripple and the overcompensation, or positive points, of ripple. Once these conditions have been satisfied, the initial assumption that they both have little effect on particle orbits can be tested.

VI Acknowledgment

The study of plasma physics at the MIT Plasma Fusion Center and specifically at the Alcator experiment is a collective effort of many individuals. Here, I wish to acknowledge those who have played a major role in both my graduate education and research.

-to Dr. Martin Greenwald, who besides being a joy to work with, helped significantly with the plasma physics involved with this thesis.

-to Professor Lawrence Lidsky, who always encouraged me and never let me lose faith in myself.

-to Dr. Boyd Blackwell, who spent many hours discussing different aspects of this work and who also taught me the powers of a computer.

-to Dr. Robert Granetz, whom I consulted about the TEX program on which this thesis was written. His endless energy for scientific work was most refreshing.

-to Susanne Strong, although not part of the group at PFC, her tireless editing and graphics work was most appreciated.

REFERENCES

[1]M. Greenwald, J.J. Schuss, D. Cope, Nucl. Fusion 20, 783 (1980).

[2]M.P.J. Gaudreau, PhD. thesis, MIT Plasma Fusion Center (Sept. 1981).

[3]Schuss et al, Phys. Rev. Lett. 43, 274 (1979).

[4]Schuss et al, Nucl. Fusion 21, 427 (1981).

[5]J.J. Schuss, T.M. Antonsen, Jr., M. Porkolab, MIT Plasma Fusion Center Report, JA-82-8 (1982).

[6]C.L. Fiore, D.P. Schissel, M.J. Greenwald, Bull. Am. Phys. Soc. 26, 885 (1981).

[7]L. Bromberg, A. Gondhalekar, MIT Plasma Fusion Center Report, RR-80-13 (1981).

[8]R.H. Fowler, D.K. Lee, P.W. Gaffney, "FLOC-Field Line and Orbit Code for the Study of Ripple Beam Injection into Tokamaks," ORNL Report TM-6293 (1978).

[9]J.M. Rawls, "Status of Tokamak Research," DOE Report ER-0034 (1979).

[10]D. Cope, S.M. thesis, MIT Plasma Fusion Center (June 1979).

[11]M. Greenwald, private communication (1980).

[12]J.W. Connor, R.J. Hastie, Nucl. Fusion 13, 221 (1973).

[13]B.B. Kadomtsev, O.P. Pogutse, Nucl. Fusion 11, 67 (1971).

[14]J. Borris, N. Winsor, "Extrapolated Numerical Integration in Theory and Practice," PPPL Report MATT-652 (1970).

[15]R. Goldston, PhD. thesis, Princeton University (April 1977).

[16]A.H. Boozer, G. Kuo-Petravic, Phys. Fluids. 24, 851 (1981).

[17]E.S.Kissel, PhD. thesis, MIT Plasma Fusion Center (June 1982).

[18]J. Schuss, private communication (1982).

[19]L.L. Carter, E.D. Cashwell, "Particle-Transport Simulation with the Monte Carlo Method," *ERDA Critical Review Series* (1975).

[20]R.W. Harvey, H.E. St. John, Bull. Am. Phys. Soc. 26, 990 (1981).

[21]F. Brown, PhD. thesis, University of Michigan (1981).

[22]C. Weggel, W. Hamburger, B. Montgomery, N. Pierce, "The Alcator C Magnetic Coil System, 12th Symposium on Engineering Problems of Fusion Research, Vol. I, Chappaqua 54 (1977).

[23]F.L. Hinton, R.D. Hazeltine, *Reviews of Plasma Physics* 48, 239 (1976).

APPENDIX A

This appendix covers the following:

(1) A description of Alcator C including a typical shot

(2) The design of Alcator C leading to ripple

A.1 Alcator description

The Alcator C tokamak is shown schematically in Figure (33). The plasma is produced and confined within a toroidal magnetic field geometry. The toroidal field is produced by external magnetic coils (Bitter Plates) while the poloidal field is generated by an induced toroidal current in the plasma. The plasma current serves a dual purpose. First, it produces the rotational transform needed for equilibrium, and, second, it ohmically heats the plasma. Due to the induced nature of the plasma current, the plasma discharge is not continuous . Typical discharges for Alcator C last 500 milliseconds. Operating parameters are as follows:

Density	$3 \times 10^{13}\, cm^{-3} - 7 \times 10^{14}\, cm^{-3}$
Electron Temperature	$700\, eV - 2500\, eV$
Ion Temperature	$500\, eV - 1500\, eV$
Current	$150\, kA - 600\, kA$
Toroidal Field	$3\, T - 10\, T$
Z_{eff}	$1.2 - 4$

The current, density, and electron temperature evolutions in time for a shot are shown in Figure (34)[17].

A.2 Design of Alcator C[22]

The Alcator C tokamak was built upon the principle that a compact device capable of achieving high magnetic fields would lead the way to reactor grade plasmas. Large volume lower field tokamaks generally have toroidal field coils built of larger bore than required

in the interest of access and reduced ripple. Alcator C can not do this without seriously reducing the achievable field. The toroidal field coil for Alcator C is a Bitter magnet design resulting in a highly uniform toroidal field because of the continuous distribution of turns. Other tokamaks have relatively few toroidal coils, when compared to Alcator C, which result in a non uniform toroidal field and a smooth sinusoidal ripple variation. The ripple in Alcator C results from an interruption of the continuous distribution of toroidal field coils. This interruption is necessary to enable access to the plasma. Diagnostic ports are provided at 60° intervals and require that the active magnetic turns be removed from a 4.0° angle at each port. This results in a toroidal field ripple of as much as 20% at the outer limiter edge. This is unacceptable, and therefore compensation must be provided. Compensation is provided in the torus by utilizing thinner turns flanking the ports. The magnitude of the field ripple is determined by the number of thin turns and their thickness. The compensation turns are designed so that they have the same average cross section at the inner diameter and are thinner at the outer diameter where the compensation is needed. This results in a ripple as shown in Figure (35). The ripple is a minimum at 68 cm.

Due to its design, the ripple is not even near sinusoidal variation. Instead there is a ripple at the diagnostic ports which varies from 1% to 5% and extends around the torus for approximately 5°. The ripple in Alcator may therefore be described as highly peaked.

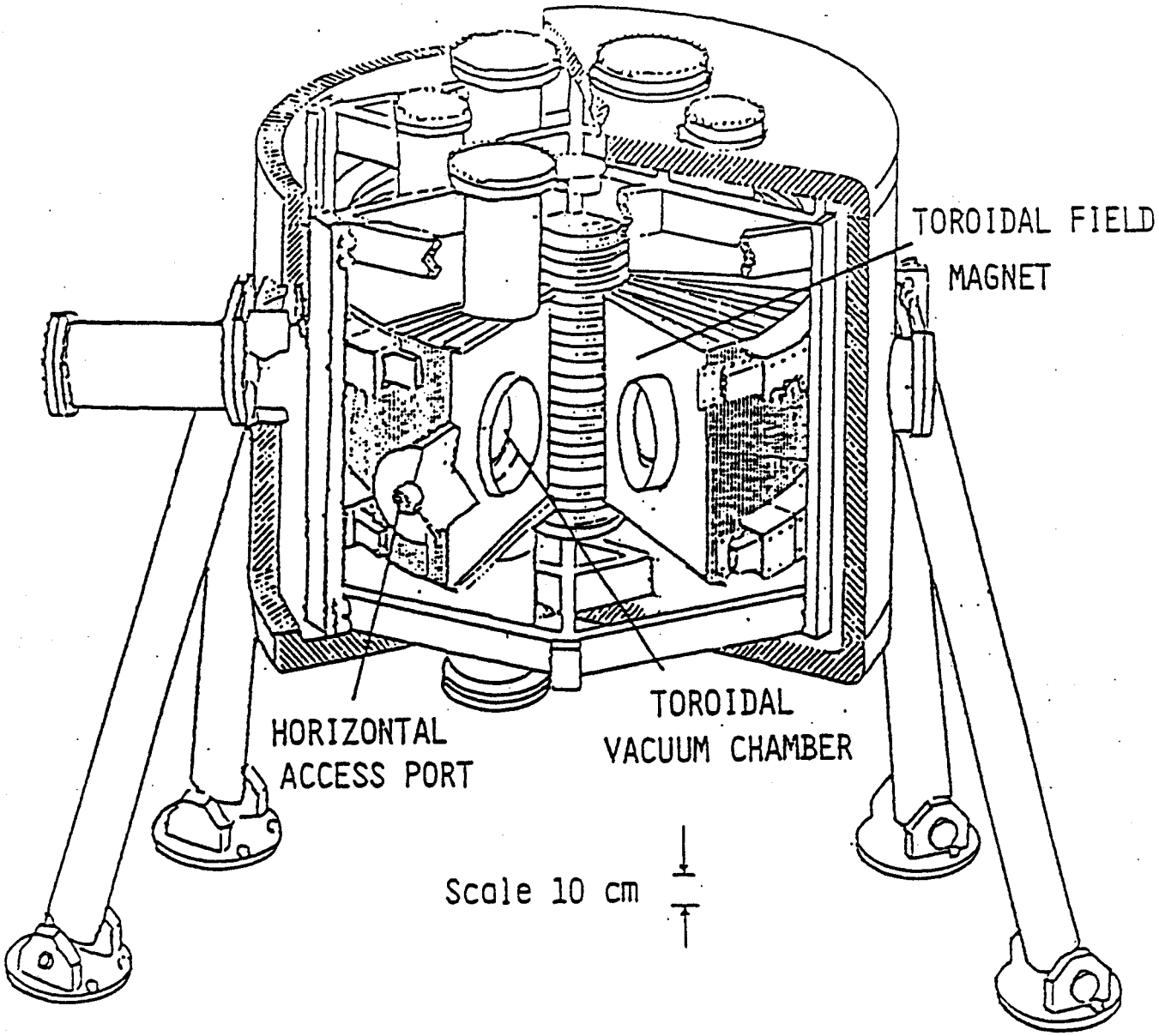

Fig. 33 — The Alcator C tokamak.

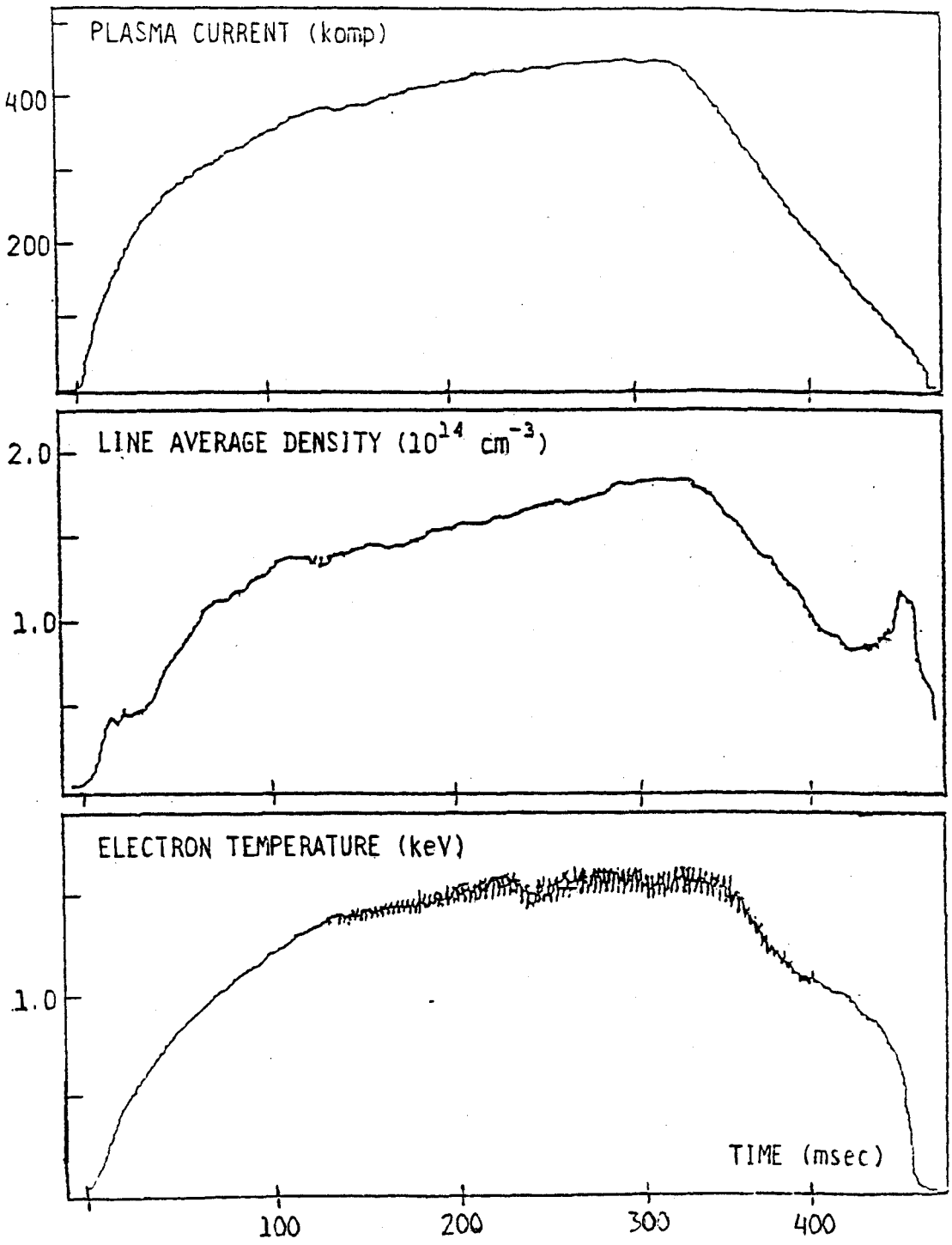

Fig. 34 — Typical time evolution of an Alcator C plasma discharge.

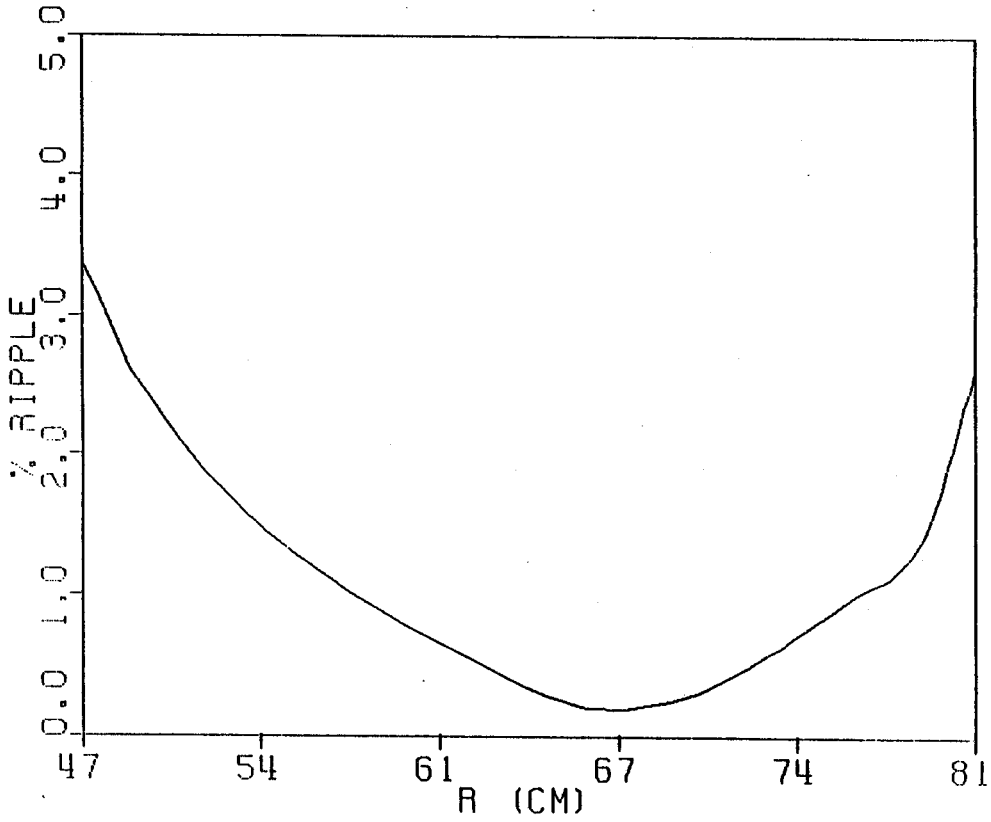

Fig. 35 — Ripple versus major radius as predicted by design studies.

APPENDIX B

This appendix covers the following derivations:

1) Pitch angle operator used in scattering

2) Energy operator used in scattering

3) Neoclassical parameters

4) Calculation of flux to the Charge Exchange Analyzer

B.1 Pitch angle operator[16]

To begin this derivation, let us first calculate the rate of change of the average pitch angle. The average pitch angle is defined by

$$\langle \lambda \rangle = \int_{-1}^{+1} \lambda f d\lambda. \tag{44}$$

The pitch angle operator is

$$\frac{\partial f}{\partial t} = \frac{\nu_d}{2} \frac{\partial}{\partial \lambda} \left(1 - \lambda^2\right) \frac{\partial f}{\partial \lambda}. \tag{45}$$

The average change in the pitch angle is

$$\frac{d\langle \lambda \rangle}{dt} = \int_{-1}^{+1} \lambda \frac{df}{dt} d\lambda. \tag{46}$$

Substituting equation (45) into equation (46) yields

$$\frac{d\langle \lambda \rangle}{dt} = \frac{\nu_d}{2} \int_{-1}^{+1} \lambda \frac{\partial}{\partial \lambda} \left(1 - \lambda^2\right) \frac{\partial f}{\partial \lambda} d\lambda. \tag{47}$$

Integrating equation (47) by parts

$$\frac{-\nu_d}{2}\int_{-1}^{+1}\left(1-\lambda^2\right)\frac{\partial f}{\partial\lambda}d\lambda, \tag{48}$$

and integrating by parts again gives

$$\frac{-\nu_d}{2}\int_{-1}^{+1}2\lambda f d\lambda = -\nu_d\langle\lambda\rangle. \tag{49}$$

Thus,

$$\frac{d\langle\lambda\rangle}{dt} = -\nu_d\langle\lambda\rangle. \tag{50}$$

Let us now calculate the rate of change of the average square of the pitch angle. The average square of the pitch angle is

$$\langle\lambda^2\rangle = \int_{-1}^{+1}\lambda^2 f d\lambda. \tag{51}$$

Taking the derivative of equation (51) and substituting equation (45) gives us

$$\frac{d\langle\lambda^2\rangle}{dt} = \frac{\nu_d}{2}\int_{-1}^{+1}\lambda^2\frac{\partial}{\partial\lambda}\left(1-\lambda^2\right)\frac{\partial f}{\partial\lambda}d\lambda. \tag{52}$$

If we now integrate by parts we may rewrite the integral as

$$-\nu_d\int_{-1}^{+1}\lambda\left(1-\lambda^2\right)\frac{\partial f}{\partial\lambda}d\lambda, \tag{53}$$

and integrating by parts again yields

$$\nu_d\int_{-1}^{+1}\left(1-3\lambda^2\right)f d\lambda. \tag{54}$$

Splitting this integral into two leaves us with an easier task. The integral over f is just 1 while the other integral is simply the average of the square of the pitch angle. This leaves us with a simple expression for the rate of change of the average of the square of the pitch angle

$$\frac{d\langle\lambda^2\rangle}{dt} = \nu_d\Big(1 - 3\langle\lambda^2\rangle\Big). \tag{55}$$

The square of the standard deviation is by definition

$$\sigma^2 = \langle\lambda^2\rangle - \langle\lambda\rangle^2. \tag{56}$$

The change of the square of standard deviation is

$$\frac{d\sigma^2}{dt} = \frac{d\langle\lambda^2\rangle}{dt} - \frac{d\langle\lambda\rangle^2}{dt}. \tag{57}$$

Realizing that

$$\frac{d\langle\lambda\rangle^2}{dt} = 2\langle\lambda\rangle\frac{d\langle\lambda\rangle}{dt}, \tag{58}$$

we may write $d\sigma^2/dt$ as

$$\frac{d\sigma^2}{dt} = \nu_d\Big(1 - 3\langle\lambda^2\rangle + 2\langle\lambda\rangle^2\Big). \tag{59}$$

If we assume that at $t = 0$ f is a delta function about $\lambda = \lambda_o$, then at $t = 0$

$$\frac{d\langle\lambda\rangle}{dt} = -\nu_d\lambda_o, \tag{60}$$

and

$$\frac{d\sigma^2}{dt} = \nu_d\Big(1 - \lambda_o^2\Big). \tag{61}$$

In a short time τ, we expect that f will be a Gaussian centered at

$$\lambda = \lambda_o(1 - \nu_d\tau), \tag{62}$$

with a standard deviation of

$$\sigma = \left[\left(1 - \lambda_o^2\right)\nu_d \tau\right]. \tag{63}$$

Therefore, we may write our pitch angle Monte Carlo operator for λ changing from λ_o to λ_n as

$$\lambda_n = \lambda_o(1 - \nu_d \tau) \pm \left[\left(1 - \lambda^2\right)\nu_d \tau\right]^{1/2}. \tag{64}$$

B.2 Energy operator[16]

Now we will derive the energy operator. The average energy is

$$\langle E \rangle = \int_0^\infty \left(\frac{1}{2} m v^2\right) f 4\pi v^2 dv. \tag{65}$$

The distribution function changes with time by

$$\frac{\partial f}{\partial t} = \frac{1}{v^2}\frac{\partial}{\partial v}\left[v^2 \nu_E \left(vf + \frac{T}{m}\frac{\partial f}{\partial v}\right)\right], \tag{66}$$

where T is the temperature of the background Maxwellian. If we take the derivative of the average energy and substitute equation (66) for $\frac{\partial f}{\partial t}$, we have

$$\frac{d\langle E \rangle}{dt} = 2\pi \int_0^\infty m v^2 \frac{\partial}{\partial v}\left[v^2 \nu_E \left(vf + \frac{T}{m}\frac{\partial f}{\partial v}\right)\right] dv. \tag{67}$$

If we perform an integration by parts and note that the product vf evaluates to zero at both $-\infty$ and $+\infty$, we have for the change in the average energy

$$-\int_0^\infty 4\pi m v^4 \nu_E f dv - 4\pi \int_0^\infty v^3 \nu_E T \frac{\partial f}{\partial v} dv = I_1 + I_2. \tag{68}$$

Integrating I_2 by parts and noting that $\partial/\partial v = mv\partial/\partial E$, we may rewrite the second integral as

$$I_2 = 2\int_0^\infty \nu_E\left[\frac{3}{2} + \frac{E}{\nu_E}\frac{d\nu_E}{dE}\right]Tf4\pi v^2 dv. \tag{69}$$

I_1 may be rewritten as

$$I_1 = -2\int_0^\infty \nu_E\left(\frac{1}{2}mv^2\right)f4\pi v^2 dv. \tag{70}$$

If we now realize that the integration is really done over a delta function in the Monte Carlo technique, then ν_E and $(E/\nu_E)\cdot(\partial\nu_E/\partial E)$ are constant and may be brought out of the integral leaving us with

$$\frac{d\langle E\rangle}{dt} = -2\nu_E\langle E\rangle + 2T\nu_E\left[\frac{3}{2} + \frac{E}{\nu_E}\frac{d\nu_E}{dE}\right]. \tag{71}$$

Let us now turn our attention to the average of the square of the energy which is given by

$$\langle E^2\rangle = \int_0^\infty \left(\frac{1}{2}mv^2\right)^2 f4\pi v^2 dv. \tag{72}$$

As before, we take the derivative of $\langle E^2\rangle$ with respect to time and substitute in the energy operator. We are left with

$$\frac{d\langle E^2\rangle}{dt} = \pi m\int_0^\infty v^4\frac{\partial}{\partial v}\left[v^2\nu_E\left(vf + \frac{T}{m}\frac{\partial f}{\partial v}\right)\right]dv. \tag{73}$$

Integrating by parts yields

$$4\pi m^2\int_0^\infty v^3\left[v^2\nu_E\left(vf + \frac{T}{m}\frac{\partial f}{\partial v}\right)\right]dv. \tag{74}$$

We may now separate the above integral into two separate ones and consider each individually

$$-4\int_0^\infty \left(\frac{1}{2}mv^2\right)^2 \nu_E f 4\pi v^2 dv - \int_0^\infty 4\pi m v^5 \nu_E T \frac{\partial f}{\partial v} dv = I_1 + I_2. \tag{75}$$

Consider, for the moment, I_2, and integrate by parts. This gives us

$$I_2 = -\int_0^\infty \left(20\pi m v^4 T \nu_E + 4\pi m v^5 T \frac{d\nu_E}{dE}\right) f dv. \tag{76}$$

We may now write our original integral as

$$I_1 + 10T\int_0^\infty \left(\frac{1}{2}mv^2\right)\nu_E f 4\pi v^2 dv + 4T\int_0^\infty \left(\frac{1}{2}mv^2\right) E \frac{d\nu_E}{dE} f 4\pi v^2 dv. \tag{77}$$

If we make the same assumption as we did before regarding the delta function f in the Monte Carlo approximation, we may do the above integrations and write

$$\frac{d\langle E^2\rangle}{dt} = -4\nu_E\langle E^2\rangle + 10T\nu_E\langle E\rangle + 4TE\frac{\partial \nu_E}{\partial E}\langle E\rangle. \tag{78}$$

As before

$$\frac{d\sigma^2}{dt} = \frac{d\langle E^2\rangle}{dt} - 2\langle E\rangle\frac{d\langle E\rangle}{dt}, \tag{79}$$

and

$$\frac{d\sigma^2}{dt} = -4\nu_E\langle E^2\rangle + 4\langle E\rangle^2\nu_E + 4T\nu_E\langle E\rangle. \tag{80}$$

If we assume as before that we have a delta function at E_o, then

$$\frac{d\langle E\rangle}{dt} = -2\nu_E E_o + 2T\nu_E\left[\frac{3}{2} + \frac{E}{\nu_E}\frac{d\nu_E}{dE}\right], \tag{81}$$

and

$$\frac{d\sigma^2}{dt} = 4T\nu_E E_o. \tag{82}$$

Thus in a short time τ, we expect f to be a Gaussian centered at

$$E = E_o - 2\nu_E\tau\left[E_o - \left(\frac{3}{2} + \frac{E}{\nu_E}\frac{d\nu_E}{dE}\right)T\right], \tag{83}$$

with a standard deviation

$$\sigma = 2(\nu_E E_o T\tau)^{1/2}. \tag{84}$$

Therefore, the energy operator for E changing from E_o to E_n is

$$E_n = E_o - 2\nu_E\tau\left[E_o - \left(\frac{3}{2} + \frac{E}{\nu_E}\frac{\partial\nu_E}{\partial E}\right)T\right] \pm 2[TE_o\nu_E\tau]^{1/2}. \tag{85}$$

B.3 Neoclassical parameters[24]

In Chapter III.2, it was stated that the trapping of particles in a tokamak occurs for the same reason as trapping occurs in a magnetic mirror. Recall that the basis for the magnetic mirror confinement scheme is the invariance in μ. As a particle moves from a weak field region to a strong field region, it sees an increasing B, and therefore $v_\perp$ must increase in order to hold μ constant. At the same time, the energy of the particle must remain constant so its $v_\parallel$ will decrease. For certain particles, $v_\parallel$ eventually becomes zero and these particles will be reflected.

With the above thoughts in mind, compare the magnetic mirror with a tokamak. In a tokamak, the magnetic field lines are helical and the toroidal field varies like $1/R$. As a particle twists around poloidally while following a field line, it sees a larger field near the inside wall and a smaller B near the outside wall. Some of the particles are trapped by the magnetic mirror effect and never circulate around the torus. As the trapped particles

guiding centers bounce back and forth along the field lines, they are also subject to a drift

$$v_D = \frac{mv_\perp^2}{2eB}\frac{\boldsymbol{B}\times\nabla\boldsymbol{B}}{B^2} + \frac{mv_\parallel^2}{eB}\frac{\boldsymbol{B}\times(\boldsymbol{B}\cdot\nabla)\boldsymbol{B}}{B^3} \tag{86}$$

arising from the inhomogeneity of the magnetic field. For a tokamak with a dominant field varying like $1/R$ the instantaneous drift is either up or down, depending on the sign of the charge and the sense of the toroidal field. As we follow the particles guiding center projection onto the poloidal plane, the part of the orbit which lies in the upper half of the torus will have an outward component of the drift in the r direction. On the lower half of the torus, the drift will have an inward component in the r direction.. The net result of these drifts is to have the guiding center projection trace out a banana; thus the so called banana orbits. Let f_t be the fraction of particles trapped; therefore $1 - f_t$ is the fraction which are untrapped. Referring to Figure (36), the untrapped fraction is given by

$$1 - f_t = \frac{1}{4\pi}\int_{\Omega_c} d\Omega_c = \frac{1}{4\pi}2\int_0^{\theta_c} 2\pi\sin\theta d\theta. \tag{87}$$

Performing the simple integration gives us that $1 - f_t = 1 - \cos\theta_c$, or that the fraction trapped is just $\cos\theta_c$. From considerations of mirror geometry, we may write that

$$\sin^2\theta_c = \frac{B_{min}}{B_{max}}. \tag{88}$$

As has been stated many times before, the main toroidal field in a tokamak has a $1/R$ dependence. Therefore

$$B_o R_o = BR, \tag{89}$$

$$\frac{B_{max}}{B_{min}} = \frac{R_{min}}{R_{max}} = \frac{R_o - r}{R_o + r}, \tag{90}$$

and

$$sin^2\theta_c = \frac{1 - r/R_o}{1 + r/R_o}. \tag{91}$$

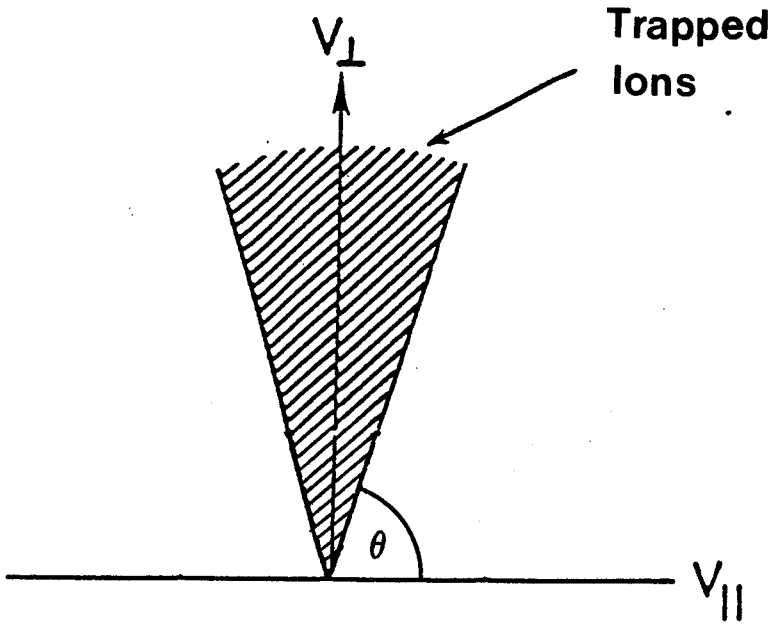

Fig. 36 — Trapped fraction of particles in velocity space.

Since r/R_o is small compared to 1, we may expand $(1 + r/R_o)^{-1}$ to $(1 - r/R_o)$. Using this expansion and keeping only terms first order of r/R_o, we have

$$sin^2\theta_c = 1 - \frac{2r}{R_o}. \tag{92}$$

The inverse aspect ratio is $\epsilon = a/R_o$. Using this as an approximation to r/R_o we may write the trapped fraction as

$$f_t = \sqrt{2\epsilon}. \tag{93}$$

The bounce time may be calculated by realizing that the force which causes the reflection is given by

$$F_{\|} = -\mu\nabla_{\|}B = -\mu\frac{\partial B}{\partial s}, \tag{94}$$

where the $\|$ indicates the direction of the magnetic field. The chain rule lets us write

$$ms'' = -\mu\frac{\partial B}{\partial s} = \mu\frac{\partial B}{\partial\theta}\frac{\partial\theta}{\partial s}, \tag{95}$$

where the θ is in physical space. The rotational transform is $q = \phi/\theta$. The arc length $s = R\phi$. Therefore

$$\frac{\partial\theta}{\partial s} = \frac{1}{Rq}, \tag{96}$$

$$B_T = \frac{R_o B_o}{R} = \frac{R_o B_o}{R_o + r\cos\theta}, \tag{97}$$

and

$$B_T = \frac{B_o}{1+\epsilon\cos\theta} \approx B_o(1-\epsilon\cos\theta). \tag{98}$$

Therefore,

$$\frac{\partial B}{\partial\theta} = B_o\epsilon\sin\theta. \tag{99}$$

Rewriting our force equation, we have

$$ms'' = -\mu B_o\epsilon\frac{1}{Rq}\sin\theta. \tag{100}$$

If we assume only small θ, therefore approximating $\sin\theta$ as θ and substituting s for θ, we have

$$s'' + \frac{\mu B_o\epsilon}{mR^2q^2}s = 0. \tag{101}$$

Realizing that this is just the equation for simple harmonic motion, we may immediately read off the frequency of motion and thus the bounce frequency of trapped particles

$$\omega_b = \frac{1}{Rq}\sqrt{\frac{\mu B\epsilon}{m}} = \frac{v_\perp}{Rq}\sqrt{\frac{\epsilon}{2}}. \tag{102}$$

In order to get an understanding of diffusion coefficients, let us first calculate the step sizes of trapped and untrapped particles. In general, we may write the equation of a perfect

circle as

$$\frac{dx}{dt} = -\omega y, \tag{103}$$

and

$$\frac{dy}{dt} = \omega x. \tag{104}$$

The circle is disturbed by v_D in the tokamak. Thus we may write

$$\frac{dy}{dt} = v_D + \omega x. \tag{105}$$

Letting $x \Rightarrow x + \delta x$ leaves us with

$$\frac{dy}{dt} = \omega x + (v_D - \omega \delta x). \tag{106}$$

The step size is then

$$\delta x = \frac{v_D}{\omega}. \tag{107}$$

For untrapped particles, ω is the poloidal orbital frequency given by

$$\omega = \frac{v_\parallel}{2\pi R q}. \tag{108}$$

The drift velocity may be written as

$$v_D = \frac{1}{2}\frac{m}{eB}\left[v_\perp^2 + 2v_\parallel^2\right]\frac{1}{R}. \tag{109}$$

Here we have assumed that

$$\nabla B = \frac{\partial B}{\partial r}, \tag{110}$$

and

$$B = \frac{B_o R_o}{R}. \tag{111}$$

Taking equations (108), (109), and substituting into equation (107) yields

$$\delta x = \frac{1}{2}\frac{mq}{eBv_{\|}}\left[v_{\perp}^2 + 2v_{\|}^2\right]. \tag{112}$$

For untrapped particles $v_{\perp} \ll v_{\|}$ and assuming that $B \approx B_T$, we have

$$\delta x = \frac{mqv_{\|}}{eB_T}. \tag{113}$$

Noting that

$$q = \frac{r}{R}\frac{B_T}{B_p} = \epsilon\frac{B_T}{B_p} \tag{114}$$

gives us the step size of untrapped particles

$$\delta x = \frac{mv_{\|}}{eB_p}\epsilon = r_{L_p}\epsilon. \tag{115}$$

For trapped particles, ω in equation (108) is the bounce frequency given by equation (102). This gives us for δx

$$\delta x = \frac{1}{2}\frac{m}{eBR}\left[v_{\perp}^2 + 2v_{\|}^2\right]Rq\sqrt{\frac{m}{\mu B\epsilon}}. \tag{116}$$

For trapped particles $v_{\perp} \gg v_{\|}$ and as before with $B \approx B_T$, we note that the step size for trapped particles, or the banana width, is

$$\delta x = \frac{1}{2}r_{L_p}\sqrt{2\epsilon}. \tag{117}$$

The step sizes just calculated can be used to better understand the diffusion coefficients. In general, a diffusion coefficient is defined by

$$D = \frac{\Delta x^2}{2\Delta t}. \tag{118}$$

For the trapped or banana particles, $\omega_b \gg \nu$ where ν is the collision frequency. The classical collision frequency for 90^o collisions is the Braginskii time ν_b. In the banana regime,

one small angle collision (ν) can be sufficient to scatter particles into the loss cone. Thus our Δt is

$$\nu = \frac{1}{\Delta t}. \tag{119}$$

Recall that

$$\cos\theta_c = \sqrt{2\epsilon}, \tag{120}$$

and thus for small angles

$$\Delta\theta = \sqrt{2\epsilon}. \tag{121}$$

Thus,

$$\nu = \frac{\nu_b}{(\Delta\theta)^2} = \frac{\nu_b}{2\epsilon}. \tag{122}$$

In the banana regime, the classical expression for the diffusion coefficient must be multiplied by the fraction trapped since we are only interested in the diffusion of these few particles. Thus for trapped particles,

$$D = \frac{\sqrt{2}}{4} r_L^2 q^2 \epsilon^{-3/2} \nu_b. \tag{123}$$

In the untrapped particle regime, $\nu = \nu_b$ since almost a 90^o collision is needed to scatter a particle into the trapped regime. Thus recalling equations (119) and (113), we have a diffusion coefficient of

$$D = \frac{1}{2} r_L^2 q^2 \nu_b. \tag{124}$$

This is called the Pfirsch-Schluter regime.

The transition regime between banana and Pfirsch-Schluter is called the Plateau regime. Slightly trapped particles with a very wide banana width dominate this regime. The diffusion coefficient here will be the coefficient for the banana regime multiplied by the

fraction slightly trapped. In this regime, ω_b is only slightly greater than ν. That fraction is

$$e^{-\nu/\omega_b} \approx 1 - \frac{\nu}{\omega_b} \approx \frac{1}{1+\nu/\omega_b}. \tag{125}$$

Using equations (119) and (102), we may rewrite the above as

$$\frac{1}{1+\frac{\nu_b Rq\sqrt{2}}{v_\perp \epsilon^{3/2}}} \approx \frac{v_\perp \epsilon^{3/2}}{\sqrt{2}\nu_b Rq}. \tag{126}$$

Taking this fraction and multiplying it by equation (123) gives us the diffusion coefficient of the Plateau regime

$$D = \frac{1}{4}\frac{r_L^2 q v_\perp}{R}. \tag{127}$$

B.4 Flux to analyzer

The rate of neutrals R produced in the plasma by charge exchange is given by

$$R = \int\int \sigma_{cx}(v_o - v_i)|v_o - v_i| f_o f_i d^3v_o d^3v_i. \tag{128}$$

Let us assume that the distribution of neutrals is a delta function in the energy region of interest. This is justified by the fact that

$$v_o \ll \sqrt{\frac{E}{m_i}}. \tag{129}$$

Thus

$$f_o = \frac{n_o \delta_o}{4\pi v_o^2}, \tag{130}$$

and, from symmetry,

$$d^3v_o = 4\pi v_o^2 dv_o, \tag{131}$$

$$d^3v_i = 4\pi v_i^2 dv_i = \frac{8\pi}{m}\sqrt{\frac{E}{2m}}dE. \tag{132}$$

Substituting (130), (131),and (132) into equation (128) and doing the integration over d^3v_o yields

$$R = \frac{8\pi n_o}{\sqrt{2}m^{3/2}} \int \sigma_{cx}(E)v(E)n_i f_i \sqrt{E}dE. \tag{133}$$

Let us further assume that $\sigma_{cx}v_i n_i f_i \sqrt{E}$ is constant over ΔE, where ΔE is the channel width. Thus

$$R = \frac{8\pi n_o}{\sqrt{2}m^{3/2}} \sigma_{cx}v_i n_i f_i \sqrt{E}\Delta E. \tag{134}$$

This flux R is the $number/sec - cm^3$ at $E \pm \frac{\Delta E}{2}$ into 4π steradians. To calculate the flux I to the analyzer, R must be corrected for the beam area, the attenuation factor, and the solid angle. If $\beta(x,E)$ is the attenuation factor from position x to the outside at a, then

$$I = \frac{\Omega A}{4\pi} \int_{-a}^{+a} \beta(x,E)Rdx. \tag{135}$$

The attenuation of flux results from any interaction which ionizes the outgoing neutral. Such reactions are charge exchange, proton ionization, and electron ionization. The sum of all these processes can be denoted as the total reaction cross section σ_T. In a distance Δx, the attenuation is

$$e^{-n_i \sigma_T \Delta x}. \tag{136}$$

For many Δx, the attenuation is

$$\beta = \prod e^{-n_i \sigma_T \Delta x} = e^{-\sum n_i \sigma_T \Delta x}, \tag{137}$$

and in the limit as $\Delta x \Rightarrow 0$,

$$\beta = e^{-\int_x^a n_i \sigma_T dx}. \tag{138}$$

Substituting equation (138) in equation (135) yields

$$I = \frac{\sqrt{2}\Omega A}{\pi^{3/2}} \int_{-a}^{+a} e^{-\int_x^a n_i(x)\sigma_T(E)dx} n_o(x) n_i(x) \sigma_{cx}(E) v(E) m f_i(E) \sqrt{E} \Delta E dx. \qquad (139)$$

APPENDIX C

This appendix covers the following:

(1) A description of the Monte Carlo code used in this thesis

(2) A description of subroutines used

(3) A list of variables used

C.1 Monte Carlo code description

The code used in this work has been written in a modular form to enable easy access to any one part. There are 6 common blocks used, and they are named for the subroutine in which they are needed. This program is written in double precision and has been running on a Digital VAX 11/780. Those variables which are used in plotting of the data are only single precision. Accompanying the code is a parameter file containing 17 initial conditions which might have to be altered from run to run. There are two loops in the program one inside the other. The first one which is encountered is called the major loop and begins at statement label 70. The code will return to label 70 only if a new particle is needed to be chosen. However, the majority of the computational time is spent in the second or integration loop which begins at statement label 200. In this loop, the field conditions are calculated at the particle position. The equations of motion are integrated, and then the particle is scattered in energy and pitch angle. Next the integration time is checked against the scattering and 90^{o} time, and altered accordingly. Following this, the data collecting bins are updated and the code returns to label 200 to begin again. The only reason for not returning to label 200 is that the particle has gone beyond the limiter radius or that the required number of interactions has been completed. If the particle has gone beyond the plasma boundary, it is treated as lost and the process for picking a new particle is begun at line 70. Data files are written out every 10^{5} interactions and also at the end of a run.

C.2 Subroutines

There are 10 subroutines involved in every computer run. Subroutine *WRITE_FILE* is called to write out a data file. Files are named runAB.dat, where the A stands for a run number and the B stands for a letter used to indicate the version of the run. Subroutine *NEW_TIME* is used to check the integration time compared to both the scattering time and the 90° time. If the integration time becomes great enough that it does not satisfy equations (32) or (33), then it is altered according to equations (34) or (35). Next, the error in μ is set to be τ_{int}/τ_{90} with a maximum of 10^{-4}. Finally, the error in the four integration variables is set to be 20% of the μ error condition. Subroutine *MAXWELL* is used to obtain the initial conditions of the particle. First of all, the particles energy is picked randomly from a Maxwellian distribution. In order to accomplish, this a data file called maxwell.dat is read and subroutines *ATSM* and *ALI* are called to order the data read in. *MAXWELL* then continues to pick the particles pitch angle and initial position. Subroutine *EXTINT* is used to integrate the equations of motion and in the process subroutines *FTEST*, *FIELD*, and *ERROR* are used. Subroutine *FTEST* contains the differential equations to be integrated. Subroutine *FIELD* contains expressions for the magnetic field, including its gradient and curl. Subroutine *ERROR* takes the error parameters set in subroutine *NEW_TIME* and uses them to check the integration of *EXTINT*. Subroutine *SCTR* is used to scatter the particle in energy and pitch angle. This subroutine is called after every integration.

C.3 Variable list

For simplicity, the variable list is divided into program blocks. Blocks include the six common statements, the main program and the ten subroutines.

(1) COMMON/FCOUNTS/

m-	Ion mass in grams
h0-	Time step used for integration by EXTINT in seconds
ch-	The charge of the ion in e.s.u.
v-	Velocity of the ion in *cm/sec*

fcount- Parameter used by EXTINT during integration

(2) COMMON/FIELD/

bα-	The magnetic field in the α direction in gauss. Directions used are $\alpha = r = r$, $\alpha = p = \phi$, and $\alpha = z = z$
gradα-	The gradient of the $b\alpha$ field
dbadβ-	The derivative of the $b\alpha$ field with respect to β
majr0-	The major radius of the tokamak R_o in cm
b0-	The toroidal field on axis B_o in gauss
a-	The limiter or minor radius of the machine in cm
q0-	The value of the safety factor at $r = 0$ q_o
qa-	The value of the safety factor at $r = a$ q_l
aa0-	The product of delta and b0. Delta is described in block (7)
mm-	The power of the cosine in the analytical ripple field model
nn-	The value of the coefficient of ϕ in the analytical ripple field model

(3) COMMON/ERRCOM/

y(20)-	The array which holds the value of the dependent variable in the equations to be integrated
s(20)-	The array which holds values corresponding to y(20) used in the error subroutine
eps-	The error condition imposed on the integration of y
rmueps-	The error condition imposed on the conservation of μ after each integration
rmuold-	The value of μ before the integration

(4) COMMON/SCATER/

pi-	The value of π
iseed-	The seed used in picking random numbers for the subroutine *SCTR*
ti-	The value of the ion temperature of the plasma T_i in eV
ne-	The value of the electron density n_e in cm^{-3}

(5) COMMON/MAXWELL/

en_arr-	The array which holds the initial energy of the ions
lambda_arr-	The array which holds the initial pitch angle of the ions
iarr-	The number of new particles picked

(6) *COMMON/WRITE_FILE/*

xaa-	The array which holds the bin number for the particles energy
tot-	The array corresponding to xaa which holds the number of counts in a bin
tot_lam-	The array corresponding to *xaa_lam* which holds the number of counts in a bin
xaa_lam-	The array which holds the bin number for the particles pitch angle
v_tot-	The array which holds the particles position on a velocity grid

a_loss- The array which holds the value of a of all lost ions. a = en = ions energy, a = lambda = λ, a = phi = ϕ, a = theta = θ, a = xxx = r/a, and a = dt = time spent to be lost

iloss- The number of particles lost

(7) MAIN PROGRAM

bmod- The magnitude of the magnetic field

delta- The coefficient of the analytic vector potential

en- The energy of the ion in eV

fact- A scaling factor used in plotting only

icount- A counter used to keep track of the number of data files

jjii- A counter used to keep track of which bin a particle is in

lambda- The pitch angle of the particle λ

majr- The value of R in cm

mmax- The number of times an extrapolation is attempted by EXTINT

nmax- The number of differential equations to be integrated

np- The total number of interactions or integration loops to be done

npp- The counter which keeps track of the number of times through the integration loop

phi- The value of ϕ in radians

vperp- The velocity of the particle which is perpendicular to the magnetic field in *cm/sec*

vpara- The velocity of the particle which is parallel to the magnetic field

x- The total time as measured in seconds from the beginning of the run

xold- The time before entering the integrator

z- The value of z in cm

(8) Subroutine *NEW_TIME*

atomic- The atomic number of the ion

coulog- The value of $\ln \Lambda$

nub- The value of the Braginskii collision frequency in sec^{-1}

nud- The deflection collision frequency

nue- The energy scattering frequency

rmueps_max- The maximum value for the error condition on μ

tau_int- The integration time in seconds

tau_scatt- The largest acceptable scattering time

tau_90- The 90^o scattering time

(9) Subroutine *SCTR*

errfnx- The value of the error function evaluated at x

dnuedx- The derivative of nue with respect to x

dxde- The derivative of x with respect to energy

sigmae- The standard deviation of the energy

sigmal- The standard deviation of the pitch angle

PLASMA FUSION CENTER INTERNAL DISTRIBUTION:

PFC BASE MAILING LIST

Argonne National Laboratory, TIS, Reports Section
Associazione EURATOM - CNEN Fusione, Italy, The Librarian
Battelle-Pacific Northwest Laboratory, Technical Info Center
Brookhaven National Laboratory, Research Library
Central Research Institute for Physics, Hungary, Preprint Library
Chinese Academy of Sciences, China, The Library
The Flinders University of S.A., Australia, Jones, Prof. LR.
General Atomic Co., Library
General Atomic Co., Overskei, Dr. D.
International Atomic Energy Agency, Austria,
Israel Atomic Energy Commission, Soreq Nucl. Res. Ctr., Israel
Kernforschungsanlage Julich, FRG, Zentralbibliothek
Kyushu University, Japan, Library
Lawrence Berkeley Laboratory, Library
Lawrence Livermore Laborary, Technical Info Center
Max-Planck-Institut fur Plasma Physik, FRG, Main Library
Nagoya University, Institute of Plasma Physics, Japan
Oak Ridge National Laboratory, Fusion Energy Div. Library
Oak Ridge National Laboratory, Derby, Roger
Physical Research Laboratory, India, Sen, Dr. Abhijit
Princeton University, PPL Library
Rensselaer Polytechnic Institute, Plasma Dynamics Lab.
South African Atomic Energy Board, S. Africa, Hayzen, Dr. A.
UKAEA, Culham Laboratory, England, Librarian
US Department of Energy, DOE Library
Universite de Montreal, Lab. de Physique des Plasmas, Canada
University of Innsbruck, Inst. of Theoretical Physics, Austria
University of Saskatchewan, Plasma Physics Lab., Canada
University of Sydney, Wills Plasma Physics Dept., Australia
University of Texas at Austin, Fusion Res. Ctr., Library
University of Wisconsin, Nucl. Eng. Dept., UW Fusion Library

INTERNAL MAILINGS

MIT Libraries
Industrial Liaison Office
G. Bekefi, A. Bers, D. Cohn, B. Coppi, R.C. Davidson,
T. Dupree, S. Foner, J. Freidberg, M.O. Hoenig, M. Kazimi,
L. Lidsky, E. Marmar, J. McCune, J. Meyer, D.B. Montgomery,
J. Moses, D. Pappas, R.R. Parker, N.T. Pierce, P. Politzer,
M. Porkolab, R. Post, H. Praddaude, D. Rose, J.C. Rose,
R.M. Rose, B.B. Schwartz, L.D. Smullin, R. Temkin, P. Wolff,
T-F. Yang